1   # A study of the dynamical characteristics of

2   # inertia–gravity waves in the Antarctic

3   # mesosphere combining the PANSY radar and a

4   # non-hydrostatic general circulation model

5

6   Ryosuke Shibuya[1] and Kaoru Sato[2]

7

8   [1] *Japan Agency for Marine-Earth Science and Technology, Yokohama, Japan*

9   [2] *Department of Earth and Planetary Science, The University of Tokyo, Tokyo,*

10   *Japan*

11

12   *Corresponding to,* Ryosuke Shibuya, Japan Agency for Marine-Earth Science and

13   Technology, 3173-25 Showa-machi, Kanazawa-ku, Yokohama, 236-0001, Japan. E-mail:

14   shibuyar@jamstec.go.jp

15

Atmospheric
Chemistry
and Physics
Discussions

Open Access

1   Abstract

2   The first long-term simulation using the high-top non-hydrostatic general circulation

3   model (NICAM) was executed to analyze mesospheric gravity waves in the period from

4   April to August in 2016. Successive runs lasting 7 days are performed using initial

5   conditions from the MERRA reanalysis data with an overlap of 2 days between

6   consecutive runs. The data for the analyses were compiled from the last 5 days of each

7   run. The simulated wind fields were closely compared to the MERRA reanalysis data and

8   to the observational data collected by a complete PANSY (Program of the Antarctic

9   Syowa MST/IS Radar) radar system installed at Syowa Station (39.6° E 69.0° S). It is

10   shown that the NICAM mesospheric wind fields are realistic, even though the amplitudes

11   of the wind disturbances appear to be larger than the radar observations.

12   The power spectrum of the meridional wind fluctuations at a height of 70 km has an

13   isolated and broad peak at frequencies slightly lower than the inertial frequency, f, for

14   latitudes from 30° S to 75° S, while another isolated peak is observed at frequencies of

15   approximately $2\pi/8$ h at latitudes from 78° S to 90° S. The spectrum of the vertical fluxes

16   of the zonal momentum also has an isolated peak at frequencies slightly lower than f at

17   latitudes from 30° S to 75° S at a height of 70 km. It is shown that these isolated peaks

18   are primarily composed of gravity waves with horizontal wavelengths of more than 1000

19   km. The latitude–height structure of the momentum fluxes indicates that the isolated

20   peaks at frequencies slightly lower than f originate from two branches of gravity wave

21   propagation paths. It is thought that one branch originates from 75° S due to topographic

22   gravity waves generated over the Antarctic Peninsula and its coast, while more than 80%

23   of the other branch originates from 45° S and includes contributions by non-orographic

Atmospheric
Chemistry
and Physics
Discussions

1   gravity waves. The existence of isolated peaks in the high-latitude region in the

2   mesosphere is likely explained by the poleward propagation of quasi-inertia–gravity

3   waves and by the accumulation of wave energies near the inertial frequency at each

4   latitude. [355 words]

5

7

8

1. Introduction

10   Waves propagating in the stably stratified atmosphere with buoyancy as a restoring

11   force are traditionally called gravity waves. Gravity waves transport momentum upward

12   from the troposphere to the middle atmosphere and are recognized as a major driving

13   force for large-scale meridional circulation in the middle-atmosphere (e.g., Fritts and

14   Alexander 2003). Because the horizontal wavelengths of significant parts of gravity

15   waves are shorter than several hundreds of kilometers, many climate models use

16   parameterization methods to calculate momentum deposition via unresolved gravity

17   waves (e.g., McFarlane 1987; Scinocca 2002; Richter et al., 2010). Currently, many

18   gravity wave parameterizations are based on very simple assumptions related to essential

19   wave dynamics, such as source spectra and propagation properties. Even though

20   physically based gravity wave parameterizations have recently been developed (e.g.,

21   Beres et al., 2004; Song and Chun 2005, Camara et al., 2014, Charron and Manzini, 2002;

22   Richter et al., 2010), tuning parameters, which are ill-defined in general circulation

23   models, such as the moving speeds of sub-grid convective cells related to the phase speeds

24   of launched gravity waves (Beres et al., 2004) or the occurrence rate for wave launching

25   for the frontogenesis function (Richter et al., 2010), still exist.

Atmospheric
Chemistry
and Physics
Discussions

1   Geller et al. (2013) showed that parameterized gravity waves in climate models are

2   not realistic in several aspects, particularly at high latitude, compared to high-resolution

3   observations and high-resolution general circulation models. Such improper

4   specifications of gravity wave momentum deposition by parameterizations are thought to

5   lead to several serious problems, such as the so-called cold-pole bias problem (Eyring et

6   al., 2010). However, many previous studies have suggested that the Antarctic region has

7   multiple types of gravity wave sources, such as the mountains of the southern Andes and

8   the Antarctic Peninsula (e.g., Eckermann and Preusse, 1999; Alexander and Teitelbaum,

9   2007; Sato et al., 2012), the small islands around the Southern Ocean (Wu et al., 2006;

10   Alexander et al., 2010; Hoffmann et al., 2013), the leeward propagation of gravity waves

11   from lower and high latitudes (Sato et al., 2009, 2012; Hindley et al., 2015), the upper

12   tropospheric jet stream (Shibuya et al., 2015; Jewtoukoff et al., 2015), and the strong polar

13   night jet (Yoshiki et al., 2000; Sato and Yoshiki, 2008; Sato et al., 2012). Therefore, these

14   processes may frequently overlap in time and space, suggesting that process-based

15   analyses based on observational data are unavoidable. In response to such recognitions of

16   the importance of gravity waves in the Antarctic, several observational campaigns in the

17   lower stratosphere have been conducted (e.g., VORCORE, Hertzog et al., 2008;

18   CONCORDIASI, Rabier et al., 2010; DEEPWAVE, Fritts et al., 2016).

19   In the Antarctic mesosphere, conversely, it is still challenging to perform

20   observations due to the harsh environment. Previous studies have used several

21   observational instruments at limited ground-based observation sites, such as medium

22   frequency (MF) radar (e.g., Dowdy et al., 2007), meteor radar (Tsutsumi et al., 1994;

23   Forbes et al., 1995), metal fluorescence LIDAR (e.g., Gardner et al., 1993; Arnold and

24   She, 2003; Chen et al., 2016), and airglow imagers (e.g., Garcia et al., 2000; Matsuda et

Atmospheric
Chemistry
and Physics
Discussions

Open Access

EGU

1   al., 2014). Using these instruments, these studies have primarily focused on the

2   temporal/spatial structures of migrating/non-migrating tides using observational data at

3   one or a couple Antarctic stations (e.g., Murphy et al., 2006, 2009; Hibbins et al., 2010)

4   and the generation/propagation mechanisms of tides using numerical models (e.g., Aso

5   2007; Talaat and Mayr 2011). However, the dominant vertical wavenumbers of gravity

6   waves have rarely been examined due to the coarse vertical resolution of the MF radars.

7   Moreover, due to the limited number of Antarctic stations, it is still very difficult to

8   examine the spatial structures of gravity waves observed in the mesosphere. Therefore,

9   discussions concerning the dynamics of gravity waves in previous studies have been

10   based on results from frequency spectrum analyses of the horizontal winds (e.g., Kovalam

11   et al., 2003) or from variance analyses of gravity wave wind fluctuations and their

12   seasonal (e.g., Hibbins et al., 2007) and interannual (e.g., Yasui et al., 2016) variations.

13   Even though a few studies using ground-based observations attempted to estimate the

14   sources of the observed mesospheric gravity waves using heuristic ray tracing methods

15   (e.g., Nicolls et al., 2010; Chen et al., 2013), a statistical analysis is required to understand

16   the dynamical characteristics of mesospheric gravity waves.

17   Observational instruments on board satellites have also been used to detect the

18   spatial distributions of temperature (radiance) data in the mesosphere (MLS: Wu and

19   Waters, 1996; Jiang et al., 2005; CRISTA: Preusse et al., 1999; Eckermann and Preusse,

20   1999; SABER: Preusse et al., 2009; Yamashita et al., 2013). In addition, Ern et al. (2011)

21   estimated the momentum flux of mesospheric gravity waves using the SABER

22   temperature data. However, the variances and momentum fluxes estimated from satellite

23   data contain contributions from a limited portion of the gravity wave spectrum due to the

24   observational filtering effects of each satellite instrument (e.g., Alexander and Barnet,

5

Atmospheric
Chemistry
and Physics
Discussions

1   2007).

2   To examine the dynamical characteristics of gravity waves, high-resolution general

3   circulation models that directly resolve a relatively wide range of the gravity wave

4   spectrum are powerful tools. At present, however, only four models have been used to

5   directly resolve mesospheric gravity waves with minimal resolved horizontal

6   wavelengths (λ_{min}) of less than 400 km and with fine vertical resolutions (dz) of less than

7   600 m in the middle atmosphere. Becker (2009) used the Kühlungsborn Mechanistic

8   General Circulation Model (KMCM) to examine the sensitivity of the state of the upper

9   mesosphere to the strength of the Lorenz energy cycle in the troposphere. Zülicke and

10   Becker (2013) used KMCM to examine the dynamical responses of the mesosphere to a

11   stratospheric sudden warming (SSW) event. In addition, by combining KMCM

12   simulations and MF radar observations in the Northern Hemisphere, Hoffman et al.

13   (2010) explored the relationship between the activities of mesospheric gravity waves and

14   critical level filtering via background wind. Liu et al. (2014) used the mesosphere-

15   resolving version of the Whole Atmosphere Community Climate Model to create a

16   horizontal map of mesospheric perturbations such as concentric gravity waves, which are

17   likely excited by deep convection in the low to middle latitudes. The KANTO model

18   (Watanabe et al. 2008) is based on the atmospheric component of version 3.2 of the Model

19   for Interdisciplinary Research on Climate (MIROC, K-1 Model Developers, 2004;

20   Nozawa et al., 2007). Sato et al. (2009) used KANTO to discuss the dominant sources of

21   mesospheric gravity waves using characteristics of the 3D momentum flux distribution.

22   Tomikawa et al. (2012) examined the dynamical mechanism of an elevated stratopause

23   event associated with an SSW event that spontaneously occurred in the KANTO model.

24   Last, the JAGUAR model is the KANTO model with the model top extended to $z_{\mathrm{top}} \cong$

Atmospheric
Chemistry
and Physics
Discussions

1   150 km including nonlocal thermodynamic equilibrium (non-LTE) for infrared radiation

2   processes. Using JAGUAR, Watanabe and Miyahara (2009) examined the dynamical

3   relationship between migrating tides and gravity wave forcing at low latitudes. Note that

4   all the current mesospheric gravity wave permitting models described above are

5   hydrostatic general circulation models.

6   As shown above, a few studies have focused on the dynamical characteristics of

7   gravity waves, such as their propagation and/or generation processes in the Antarctic

8   mesosphere. However, no study has attempted to simulate mesospheric gravity waves

9   whose reality is confirmed via high-resolution observations. This is partially because

10   there are few observational instruments with a sufficiently high resolution to validate

11   mesospheric gravity waves simulated in models. Therefore, the dynamical characteristics

12   of gravity waves observed in the Antarctic mesosphere have not been fully examined

13   using both observations and numerical simulations.

14   This study uses two novel methods. One is the first Mesosphere–Stratosphere–

15   Troposphere/Incoherent Scattering (MST/IS) radar in the Antarctic, which was recently

16   installed at Syowa Station (39.6° E 69.0° S) by the "Program of the Antarctic SYowa

17   MST/IS radar" project (the PANSY radar, Sato et al., 2014). The PANSY radar is the only

18   observational instrument in the Antarctic capable of capturing the fine vertical structures

19   of horizontal and vertical mesospheric wind disturbances when the mesosphere is ionized,

20   primarily by solar radiation during the daytime. This means that the observational data

21   from the PANSY radar can be used to validate the results of mesospheric gravity wave

22   permitting models at fine vertical resolution. Furthermore, this study uses the high-top

23   version (Shibuya et al., 2017) of the Non-hydrostatic ICosahedral Atmospheric Model

24   (NICAM; Satoh et al., 2014). This is a global cloud-resolving model with a non-

1 hydrostatic dynamical core with icosahedral grids. Such a non-hydrostatic model is likely

2 preferable for simulations of the high-intrinsic-frequency gravity waves contributing to a

3 large portion of the momentum flux convergence in the upper-middle atmosphere (e.g.,

4 Reid and Vincent, 1987; Fritts and Vincent, 1987; Fritts 2000, Sato et al. 2017). Moreover,

5 gravity waves generated by deep convection are expected to be correctly resolved in non-

6 hydrostatic models.

7   Recently, using continuous PANSY radar observations of polar mesosphere summer

8 echoes (PMWEs) at heights from 81 km to 93 km, Sato et al. (2017) showed that relatively

9 low-frequency disturbances from 1 d^{-1} to 1 h^{-1} primarily contribute to the zonal and

10 meridional momentum fluxes. This study examines the dynamical characteristics of

11 gravity waves with relatively low frequency in the Antarctic mesosphere, such as the

12 wave parameters, propagation, and generation mechanisms, via a long-term simulation

13 using the high-top high-resolution non-hydrostatic general circulation model for five

14 months from April to August in 2016. The simulated wind fields are closely compared to

15 the PANSY radar observations at small scales and the MERRA reanalysis data at large

16 scales. In addition, the statistical characteristics of the mesospheric disturbances

17 simulated by NICAM, such as the frequency (ω) spectra of each variable, the kinetic and

18 potential energies, and the momentum and energy fluxes of the gravity waves, are

19 examined.

20   This paper is organized as follows. The methodology is described in Section 2. The

21 numerical results are compared to the observational results in Section 3. The gravity wave

22 characteristics are examined based on a spectrum analysis in Section 4. A discussion is

23 presented in Section 5, and Section 6 summarizes the results and provides concluding

24 remarks.

Atmospheric
Chemistry
and Physics
Discussions

1

2. Methodology

2.1. The PANSY radar observations

The PANSY radar is the first MST/IS radar in the Antarctic and is installed at Syowa

Station (39.6° E 69.0° S) to observe the Antarctic atmosphere in the height range from

1.5 km to 500 km. Note that an observational gap exists from 25 km to 60 km due to the

lack of backscatter echoes in this height region (Sato et al., 2014). The PANSY radar

employs a pulse-modulated monostatic Doppler radar system with an active phased array

consisting of 1045 crossed-Yagi antennas. The PANSY radar observations of the 3D

winds have standard time and height resolutions along the beam direction of Δt = ~1

min and Δz = 150 m, respectively, for the troposphere and lower stratosphere, and Δt

= ~1 min and Δz = 300–600 m, respectively, for the mesosphere. The accuracy of the

line-of-sight wind velocity is approximately 0.1 m s^{-1}. Because the target of the MST

radars is the atmospheric turbulence, wind measurements can be made under all weather

conditions. Continuous observations have been made by a partial PANSY radar system

since April 30, 2012, and by a full system since October 2015. See Sato et al. (2014) for

further details concerning the PANSY radar system.

The PANSY radar data that we used are line-of-sight wind velocities of five vertical

beams in the vertical direction and tilted east, west, north, and south at a zenith angle of

θ = 10° for the period of April–May 2016, during which the PANSY radar frequently

detected the PMWEs at heights of 60–80 km (Nishiyama et al., 2015). The vertical wind

component is directly estimated from the vertical beam. The zonal wind component is

obtained using a pair of line-of-sight velocities from the east and west beams. The line-

of-sight velocities of the east and west beams, $V_{\pm\theta}$, are composed of the zonal and

vertical components of the wind velocity $(u_{\pm\theta}, w_{\pm\theta})$ in a targeted volume range:

5
$$V_{\pm\theta} = \pm u_{\pm\theta} \sin\theta + w_{\pm\theta} \cos\theta.$$

1   Assuming that the wind field is homogeneous at each height, i.e., $u_{+\theta} = u_{-\theta} \equiv u$ and

2    $w_{+\theta} = w_{-\theta} \equiv w$, we can estimate zonal wind component as

6
$$u = \frac{V_{+\theta} - V_{-\theta}}{2\sin\theta}.$$

3   The meridional wind component is estimated in the same way using the north and south

4   beams.

7

8   2.2. Numerical setup for the non-hydrostatic model simulation

9   The simulation was performed using the NICAM, which a global cloud-resolving

10   model (Satoh et al., 2008, Satoh et al., 2014). The non-hydrostatic dynamical core of the

11   NICAM was developed using icosahedral grids modified via the spring dynamics method

12   (Tomita et al., 2002). The simulation period is from March 20 to August 31, 2016.

13

14   2.2.1. Grid coordinate system and physical schemes

15   The resolutions of the horizontal icosahedral grids are represented by g-level n (grid

16   division level n). G-level 0 denotes the original icosahedron. By recursively dividing each

17   triangle into four smaller triangles, a higher resolution is obtained. The total number of

18   grid points is $N_g = 10 \cdot 4^n + 2$ for g-level n. The actual resolution corresponds to the

19   square root of the averaged control volume area, $\Delta x \equiv \sqrt{4\pi R_E^2/N_g}$, where R_E is the

20   Earth's radius. A g-level 8 grid is used in this study ($\Delta x \sim 28$ km).

21   Recently, Shibuya et al. (2016) developed a new icosahedral grid configuration that

22   has a quasi-uniform and regionally fine mesh within a circular region using spring

23   dynamics. This method clusters grid points over a sphere into a circular region (the

24   targeted region). By introducing sets of mathematical constraints, it has been shown that

1 the minimum resolution within the targeted region is uniquely determined by the area of

2 the targeted region. In this study, the targeted region for a given g-level is a region south

3 of 30° S centered on the South Pole, corresponding to a horizontal resolution of

4 approximately 18 km in the targeted region.

5   To finely simulate the structures of the disturbances in the stratosphere and the

6 mesosphere, the vertical grid spacing is set to 300 m at heights from 2.4 km to 80 km.

7 Note that, according to Watanabe et al. (2015), the gravity wave momentum flux is not

8 heavily dependent on the vertical spacing of the model in the middle atmosphere when

9 $\Delta z < 400$ m. The number of vertical grids is 288. To prevent unphysical wave reflections

10 at the top of the boundary, a 7-km-thick sponge layer is set above z = 80 km. Second-

11 order Laplacian horizontal hyper-viscosity diffusion and Rayleigh damping for the

12 vertical velocity are used in the sponge layer. The *e*-folding time of the ∇^2 horizontal

13 diffusion for a $2\Delta x$ wave at the top of the model is 4 s, and the *e*-folding time of Rayleigh

14 damping for the vertical velocity at the top of the model is 216 s. The diffusivity level

15 gradually increases from the bottom to the top of the sponge layer. We confirmed that

16 little wave reflection near the sponge layer occurs under this setting (not shown). In

17 addition, to prevent numerical instabilities in the model domain, sixth-order Laplacian

18 horizontal hyper-viscosity diffusion is used over the entire height region. The *e*-folding

19 time of the ∇^6 horizontal diffusion for a $2\Delta x$ wave at the top of the model is

20 approximately 2 s. This means that the high-top NICAM model can resolve gravity waves

21 with horizontal wavelengths longer than approximately 250 km. Table 1 summarizes the

22 physical schemes used in this study. No cumulous or gravity wave parameterizations were

23 employed. Note that this model does not use the nudging method as an external forcing

24 for the atmospheric component.

Atmospheric
Chemistry
and Physics
Discussions

1

2   2.2.2. Initial condition and time integration technique

3   MERRA reanalysis data based on the Goddard Earth Observing System Data

4   Analysis System, Version 5 (GEOS-5 DAS; Rienecker et al. 2011), is used as the initial

5   condition for the atmosphere. The initial data for the land surface and slab ocean models

6   were interpolated from the 1.0°-gridded National Centers for Environmental Prediction

7   final analysis. In the MERRA reanalysis data, the following two types of 3D fields are

8   provided: one produced using the corrector segment of the Incremental Analysis Update

9   (IAU, Bloom et al., 1996) cycle (1.25° × 1.25° with 42 vertical levels whose top is 0.1

10   hPa) and the other pertaining to fields resulting from the Gridpoint Statistical

11   Interpolation analyses (GSI analysis, e.g., Wu et al., 2002) on a native horizontal grid

12   with native model vertical levels (0.75° × 0.75° with 72 vertical levels whose top is 0.01

13   hPa). We use the former 3D assimilated fields from 1000 hPa to 0.1 hPa and the latter 3D

14   analyzed fields from 0.1 hPa to 0.01 hPa for the initial conditions of the NICAM

15   simulation to prepare realistic atmospheric fields in the mesosphere. The latter 3D

16   analyzed fields were only used at heights above 0.1 hPa because variables for the vertical

17   pressure velocity, cloud liquid water, and ice mixing ratios are not included. The vertical

18   pressure velocities, cloud liquid water, and ice mixing ratios above 0.1 hPa were set to

19   zero. The time step was 15 s, and the model output was recorded every hour.

20   Time integrations were performed following a technique similar to Plougonven et al.

21   (2013) to maintain long-term simulations sufficiently close to the reanalysis data. The

22   time integration method is illustrated in Fig. 1. Simulations lasted 7 d for each run with

23   initial conditions from the MERRA reanalysis data with an overlap of 2 day between each

24   run. The two-day overlap consists of the spin up time for the subsequent simulation. The

1 successive data for the analyses were compiled using the data from the last 5 days of each

2 run. This method allows the model to freely produce gravity waves and mesoscale

3 phenomena without artifacts caused by nudging and assimilation techniques. However,

4 because the successive simulation data are not continuous, spurious and drastic gaps in

5 the atmospheric fields between two consecutive simulations may appear. Therefore, in

6 this study, the statistical analyses are performed by taking an average of the results using

7 the respective five-day simulations to avoid any influences from gaps between the

8 simulations. A long-term continuous run from a single initial condition was not performed

9 because the model fields tend to diverge from the actual atmosphere without appropriate

10 parameterization methods and/or nudging or assimilation techniques.

11

12 **3. Results and comparisons of the numerical simulations**

13 3.1. Wave structures in the mesosphere

14 Figure 2 shows time–height sections of the line-of-sight winds observed by the north

15 beam of the PANSY radar ($V_N = v \sin \theta + w \cos \theta$, where $\theta = 10°$) and V_N calculated

16 using v and w simulated by NICAM for May 10–20, 2016. The missing values in the

17 PANSY radar observation are shown in white. The black dotted vertical lines in Fig. 2b

18 indicate the segments of the continuous five-day simulations. In the middle of May, large

19 amounts of observational data from the PANSY radar are available because strong

20 PMWEs were observed in the daytime during this period.

21 At heights of 60–75 km, negative V_N values are dominant during the observed

22 periods, which is consistent with mesospheric residual circulation in the winter

23 hemisphere. On May 13 and 16, it appears that disturbances with negative vertical phase

24 speeds are dominant in the height range of 75–80 km. These features are also observed in

1   the model data in Fig. 2b. The downward-propagating disturbances have positive V_N

2   values at heights of 75–80 km on May 13 and 16, as in Fig. 2a. Therefore, the overall

3   wave structures are well reproduced by NICAM. However, the phases of the disturbances

4   on May 13 are different from the observations. This is likely because this is the final day

5   of the seven-day integration from the initial condition (Fig. 1). The large-scale fields

6   likely do not remain sufficiently close to the reanalysis data after such a long simulation

7   time.

8   To quantitatively compare the wave structures observed by the PANSY radar and

9   those simulated by NICAM, the amplitudes of the wave disturbances were estimated as a

10   function of the vertical phase velocities. Figures 3a and 3b show time–height sections of

11   the line-of-sight winds observed by north beam of the PANSY radar for April 26–28

12   and a close up for April 28, 2016, respectively. The vertical phase velocity V_1 is used to

13   illustrate this estimation method. Here, phase lines with a vertical phase velocity of V_1

14   at heights of 65–80 km from 0400 UTC to 1800 UTC are defined as $L_1, L_2, \ldots, L_i, \ldots L_N$

15   (denoted by the black lines in Fig. 3b) and sets of data points on L_i $(x_1^i, x_2^i, \ldots, x_{n_i}^i$; the

16   black circles in Fig. 3b) are defined as $\mathcal{L}_i$ $(x_1^i, x_2^i, \ldots, x_{n_i}^i \in L_i)$. The estimated

17   amplitude A of disturbances with the vertical phase velocity V_1 is defined by

18   calculating the average of the covariances of $\mathcal{L}_1, \mathcal{L}_2 \ldots \mathcal{L}_N$:

$$A^2 = 2.0 \times \left[\left. \left(\sum_k \left(\sum_{i \geq j} x_i^k x_j^k \, (i, j \in \mathcal{L}_k) \right) \right) \middle/ \sum_k \left(\sum_{i \geq j} 1 \, (i, j \in \mathcal{L}_k) \right) \right]. \qquad (1)$$

19   When the disturbance is due to a monochromatic wave defined by V_1 ($\psi =$

20   $a \cos(imz - i\omega t)$ where $\omega/m = V_1$), the estimated amplitude A is equal to the

21   amplitude of the monochromatic wave a via the factor of 2.0 introduced on the right

22   hand side of the equation. However, the estimated amplitude A becomes very small

1   when phase lines with the vertical phase velocity do not match the wave structure (V_2, the

2   red lines in Fig. 3b). Therefore, the estimated magnitude A has a peak at the dominant

3   vertical phase velocity of the wave disturbances. The main advantage of this method is

4   that it can easily be applied to both simulated data and observed data that have missing

5   values, as in the PANSY radar observations. Prior to the application of this method, a

6   bandpass filter is applied to the observed/simulated northward line-of-sight winds with

7   cutoff wave periods of 2 h and 60 h to extract the dominant wave-like structures. In this

8   study, the estimation method for the PANSY radar observation is only applied to data on

9   days in which the ratio of the available data points in a period from 0400 UTC to 1800

10   UTC and at heights of 65–80 km exceeds 60% (April 25 and 26 in Fig. 3a). In April and

11   May, PANSY radar observation data were available for this method on 12 days and 16

12   days, respectively.

13   Figures 4a and 4b show the estimated amplitude as a function of the vertical

14   downward phase velocity in April and May using data from the PANSY radar

15   observations and the NICAM simulations, respectively. In Fig. 4a, it appears that the

16   dominant wave disturbances observed by the PANSY radar have vertical phase velocities

17   of approximately 0.5 m s^{-1} and 0.7 m s^{-1} in April and May, respectively. These features

18   are well simulated by the NICAM simulations (Fig. 4b). Therefore, the dominant wave

19   structures in the time–altitude section in the NICAM simulations are likely very similar

20   to those observed by the PANSY radar. However, the mesospheric disturbances simulated

21   by NICAM have an approximately 3.5 times larger amplitude than those observed by the

22   PANSY radar. Using a hodograph analysis, Shibuya et al. (2017) showed that NICAM

23   simulations overestimate wave amplitudes by approximately 1.5 times compared to the

24   PANSY radar observations in the mesosphere. As mentioned in Section 2.2.1, the high-

1   top NICAM only resolves gravity waves with horizontal wavelengths shorter than

2   approximately 250 km. Such a strong horizontal diffusion may cause the mesospheric

3   wave structures in NICAM to be overly monochromatic compared to the PANSY radar

4   observations, likely leading to the overestimation of the wave amplitudes in this analysis.

5

6   3.2. Zonal wind components from the troposphere to the mesosphere

7   Next, zonal wind components simulated by NICAM are compared to those in the

8   MERRA reanalysis data. Figure 5 shows time–altitude cross sections of the zonal winds

9   from the MERRA reanalysis data and from the NICAM simulations for the period of May

10 10–20, 2016, at a grid near Syowa Station. In Fig. 5b, gaps between the continuous five-

11 day simulations are observed in the troposphere and the lower stratosphere. This is likely

12 because the large-scale flows diverge from the MERRA reanalysis data during the seven-

13 day integrations. Nevertheless, roughly speaking, the disturbances in the troposphere and

14 lower stratosphere are successfully simulated by NICAM. Conversely, in the upper

15 stratosphere and mesosphere, large-amplitude disturbances with negative vertical phase

16 speeds are clear in the NICAM data but rarely seen in the MERRA reanalysis data.

17 Therefore, to validate the dynamical characteristics of the mesospheric disturbances

18 simulated by NICAM, observational data with high vertical and temporal resolution, such

19 as data from the PANSY radar, are required.

20   In addition, the latitude–altitude structures of the mean zonal winds in May 2016

21 between the MERRA reanalysis data and the NICAM simulations are compared in Fig.

22 6. In May 2016, it appears that the polar night jet in the upper stratosphere and mesosphere

23 tilts equatorward with height. Such a feature is successfully simulated by NICAM. In

24 particular, the structure of the polar night jet below 35 km in NICAM agrees with that in

Atmospheric
Chemistry
and Physics
Discussions

Open Access

1   MERRA. However, the magnitude of the zonal wind around the core of the polar night

2   jet in NICAM is slightly larger than that in MERRA. Moreover, the axis of the polar night

3   jet in the mesosphere in NICAM does not tilt strongly equatorward with height as it does

4   in MERRA. Therefore, the zonal momentum balance in the mesosphere at the initial

5   conditions is not completely maintained in NICAM, likely due to unresolved gravity

6   waves with short horizontal wavelengths. Even though some discrepancies are observed

7   in the mesosphere, the structure of the polar night jet in NICAM is sufficiently close to

8   that in MERRA. Hereafter, analyses of the gravity wave characteristics are performed

9   using data for the time period of June 1–August 31, 2016 (JJA).

10

11   **4. Gravity wave characteristics in the mesosphere**

12   4.1. Gravity wave energy and momentum fluxes

13   In this subsection, the spatial structures of the kinetic and potential energies and the

14   momentum and energy fluxes of the gravity waves are examined. The gravity wave

15   component is defined as wave components with frequencies higher than $2\pi/30$ h. Note

16   that previous studies have defined the planetary wave component to have frequencies

17   lower than approximately $2\pi/40$ h in the mesosphere (e.g., Murphy et al., 2007;

18   Baumgaertner et al., 2008).

19   In the linear theory of inertia–gravity waves that assumes the following form,

$$\left(u', v', w', \frac{p'}{\bar{p}}, \frac{\rho'}{\bar{\rho}}, \frac{\theta'}{\bar{\theta}}\right)$$
$$= \left(\tilde{u}, \tilde{v}, \tilde{w}, \tilde{p}, \tilde{\rho}, \tilde{\theta}\right)\exp(kx + ly + mz - \omega t), \tag{2}$$

20   where $\tilde{\ }$ denotes the Fourier transform of each variable, the polarization relationships

21   for the different variables are written as

$$\tilde{u} = \left(\frac{i\widehat{\omega}k - fl}{i\widehat{\omega}l + fk}\right)\tilde{v}, \tag{3}$$

$$\tilde{p} = \left(\frac{\hat{\omega}^2 - f^2}{\hat{\omega}k + ifl} \right) \tilde{u},$$

and

$$\tilde{w} = -\frac{m\hat{\omega}}{N^2 - \hat{\omega}^2} \tilde{p}.$$

1 Using these relationships, the real component of the zonal and meridional components of

2 the vertical momentum flux $(\overline{u'w'}, \overline{v'w'})$ and that of the horizontal momentum flux

3 $(\overline{u'v'})$ are expressed as

$$(\overline{u'w'}, \overline{v'w'}) = -\frac{N^2 - \hat{\omega}^2}{\hat{\omega}^2 - f^2} \cdot \frac{1}{m} (k, l) \cdot \tilde{\overline{w}}^2,$$

$$(4)$$

and

$$\overline{u'v'} = kl \cdot \frac{\hat{\omega}^2 - f^2}{f^2 k^2 + \hat{\omega}^2 l^2} \cdot \tilde{\overline{v}}^2.$$

4 Because $(N^2 - \hat{\omega}^2)/(\hat{\omega}^2 - f^2) > 0$ and $\hat{\omega}^2 - f^2 > 0$ for inertia–gravity waves, the

5 signs of $(\overline{u'w'}, \overline{v'w'})$ are equal to those of (k, l) for upward energy propagating waves

6 (i.e., $m < 0$) and the sign of $\overline{u'v'}$ is equal to that of $(k \cdot l)$. The horizontal intrinsic

7 group velocities of the gravity wave are written as

$$\left(\hat{C}_{gx}, \hat{C}_{gy} \right) = \frac{[k(N^2 - \hat{\omega}^2), l(N^2 - \hat{\omega}^2)]}{\hat{\omega}(k^2 + l^2 + m^2)}.$$

$$(5)$$

8 Therefore, the directions of the group velocities relative to the mean wind are also inferred

9 from the signs of the momentum fluxes. Note that this derivation is based on the

10 assumption of monochromaticity for the inertia–gravity wave.

11   Figure 7 shows horizontal maps of the zonal wind (U), the kinetic energy $(\overline{KE} =$

12 $\frac{1}{2}(\overline{u'^2} + \overline{v'^2} + \overline{w'^2}))$, and the potential energy $(\overline{PE} = \frac{1}{2} \frac{g^2}{N^2} \overline{\left(\frac{\theta'}{\bar{\theta}} \right)^2})$ divided by the density,

13 $\overline{u'w'}$, $\overline{v'w'}$, and $\overline{u'v'}$ at heights of 25 km, 55 km, and 70 km averaged over JJA. For the

14 estimation of $\overline{PE}$, the fluctuation of the potential temperature is calculated as

$$\frac{\theta'}{\bar{\theta}} = \frac{1}{\rho_0} \left(\frac{p'}{c_s^2} - \rho' \right),$$

$$(6)$$

15 where c_s denotes the speed of sound in the atmosphere. The axis of the polar night jet

18

Atmospheric
Chemistry
and Physics
Discussions

1   tilts equatorward with height, as seen in Fig. 6. For $\overline{KE}$ and $\overline{PE}$ at a height of 25 km,

2   large energies are distributed near 30° S and along the jet axis at approximately 60° S.

3   Localized energy peaks are also seen over the Antarctic Peninsula and the southern Andes

4   and their leeward region, which is consistent with the result of the KANTO model (Sato

5   et al., 2012). For $\overline{KE}$ and $\overline{PE}$ at heights of 55 km and 70 km, large values are observed

6   along latitudinal circles roughly corresponding to the axis of the polar night jet. Strictly

7   speaking, the large values of $\overline{KE}$ and $\overline{PE}$ at a height of 55 km appear to be distributed

8   slightly poleward of the axis of the polar night jet, while those of $\overline{KE}$ at a height of 70

9   km are broadly distributed but are primarily poleward of 60° S. It is interesting that the

10   largest energies are seen near 180° E at heights of 55 km and 70 km.

11   At a height of 25 km, $\overline{u'w'}$ is primarily negative and large values are seen over both

12   the Antarctic Peninsula and the southern Andes. Conversely, $\overline{v'w'}$ is primarily positive

13   over the Antarctic Peninsula and negative over the southern Andes. This result suggests

14   the existence of wave-like structures with phases aligned in the northwest–southeast

15   direction over the southern Andes and in the northeast–southwest direction over the

16   Antarctic Peninsula, which is confirmed by previous observational studies (e.g.,

17   Alexander and Barnet, 2007) and by numerical models (e.g., Sato et al., 2012; Plougonven

18   et al., 2013). At higher altitudes, negative values of $\overline{u'w'}$ are distributed along the

19   latitudinal circle near 60° S at a height of 55 km and near 50° S at 70 km. Note that the

20   large negative values over the southern Andes and its leeward region are observed even

21   at a height of 70 km. The signs of $\overline{v'w'}$ are primarily negative along and equatorward of

22   the polar night jet axis and positive or weakly negative poleward of the jet axis at 25 km.

23   This may indicate that the gravity waves propagate into the polar night jet as shown in

24   Sato et al. (2009). The sign of $\overline{u'v'}$ is primarily positive at heights of 55 km and 70 km,

Atmospheric
Chemistry
and Physics
Discussions

1   while it is positive equatorward of 60° S and negative poleward of 60° S at 25 km. These

2   features are consistent with the distributions of $\overline{u'w'}$ and $\overline{v'w'}$ (Eq. (4)). Therefore, it is

3   suggested that the statistical characteristics of disturbances defined as components with

4   wave frequencies higher than $2\pi/30$ h follow linear relationships of the inertia–gravity

5   waves.

6

7   4.2. Spectrum analysis

8   4.2.1. The meridional structure of the power spectra

9   To examine the statistical characteristics of the mesospheric disturbances simulated

10   by NICAM, the ω power spectra of u, v, w, and the temperature ($P_u(\omega)$, $P_v(\omega)$,

11    $P_w(\omega)$, and $P_{\text{tem}}(\omega)$, respectively) were obtained for the period of JJA 2016. The power

12   spectra were examined using the Blackman–Tukey (1958) method (e.g., Sato 1990). First,

13   an autocorrelation function was calculated for each five-day simulation to avoid any

14   influences of the gaps between the segments of the simulations. Second, to reduce

15   statistical noise in the power spectra estimation, the autocorrelation functions were

16   averaged over JJA. The maximum lag in the calculation of the autocorrelation function

17   was set to 90 h to increase the frequency resolution of the ω spectra; this is 75% of the

18   simulation period (120 h) in each segment.

19   Figure 8 shows $P_u(\omega)$, $P_v(\omega)$, $P_w(\omega)$, and $P_{tem}(\omega)$ for JJA averaged over

20   heights of 70–75 km at a grid point near Syowa Station. It is seen that $P_u(\omega)$ and $P_v(\omega)$

21   have isolated peaks at a frequency of $2\pi/12$ h, while they obey a power law with an

22   exponent of approximately −5/3 for frequencies higher than $2\pi/12$ h. Such a power law

23   structure in the high-frequency region is consistent with previous observational studies

24   by MST radars at mid-latitudes (e.g., Muraoka et al., 1990) and in the Antarctic (Sato et

25   al., 2017). Conversely, $P_w(\omega)$ has a flat structure (i.e., $\propto \omega^0$) for frequencies from $2\pi/2$

Atmospheric
Chemistry
and Physics
Discussions

1   h to $2\pi/5$ d and has no clear spectral peak. Finally, $P_{tem}(\omega)$ does not have a clear peak

2   at the frequency of $2\pi/12$ h but rather a broad peak at frequencies near $2\pi/10$ h. The

3   spectral slope of $P_{tem}(\omega)$ is steeper than $-5/3$ but gentler than -1 in the high-frequency

4   region.

5   Next, the zonally averaged v power spectra $(P_v(\omega))$ in JJA without the diurnal

6   and semi-diurnal migrating tides and the semi-diurnal non-migrating tides with $s = 1$

7   was calculated to examine the non-tidal low-frequency disturbances (Sato et al., 2017).

8   Hereafter, $P_v(\omega)$ without these tides is denoted $\widetilde{P}_v(\omega)$. The zonal mean $\widetilde{P}_v(\omega)$ in JJA

9   is shown as a function of the latitude for the heights of 70 km, 55 km, 40 km, and 25 km

10   in Figs. 9a, 9b, 9c, and 9d, respectively. The temperature power spectra $(\tilde{P}_{\text{tem}}(\omega))$ at a

11   height of 70 km are also shown in Fig. 9e. The thick red dashed curves indicate the inertial

12   frequencies at each latitude.

13   At a height of 70 km, the spectral peaks appear at frequencies slightly lower than the

14   inertial frequencies from 65° S to 75° S, as in Fig. 9a. In the mid-latitudes, the spectral

15   values are maximized near $2\pi/24$ h. Conversely, in regions from 77° S to 90° S, the

16   spectral peaks are seen near frequencies from $2\pi/8$ h to $2\pi/10$ h but are absent at $2\pi/12$ h

17   (and at the inertial frequencies) or $2\pi/24$ h. Such peaks near frequencies from $2\pi/8$ h to

18    $2\pi/10$ h in the high-latitude region also appear in $\tilde{P}_{\text{tem}}(\omega)$ (Fig. 9e).

19   The spectral peaks near the inertia frequency are also found in the high-latitude

20   region at a height of 55 km (Fig. 9b). In addition, large spectral values are distributed in

21   the frequency range from the inertial frequencies to $2\pi/24$ h from 50° S to 60° S but not

22   from 30° S to 40° S. The spectral peaks near the inertia-frequency in the high-latitude

23   region are barely seen at heights of 40 km and 25 km, suggesting that such spectral peaks

24   in the high-latitude region are only found in the mesosphere. At a height of 25 km, the

Atmospheric
Chemistry
and Physics
Discussions

1   spectral values are greatest in the inertial frequencies at mid-latitudes from 30° S to 40°

2   S, which is consistent with the result shown by Sato et al. (1999) using a high-resolution

3   GCM. Note that energy peaks at frequencies from $2\pi/10$ h to $2\pi/8$ h in regions from 77°

4   S to 90° S are seen at all heights.

5   Here, we focus on the spectral peaks found in Fig. 9a near the inertial frequency

6   from 65° S to 75° S and at frequencies from $2\pi/10$ h to $2\pi/8$ h from 77° S to 90° S. The

7   horizontal map of the integration of $\widetilde{P}_v(\omega)$ (i.e., the variance) for frequencies from $2\pi/30$

8   h to $2\pi/12$ h at a height of 70 km is shown in Fig. 10a, while that at frequencies from

9    $2\pi/12$ h to $2\pi/6$ h is shown in Fig. 10b. It appears that variances for frequencies from

10    $2\pi/30$ h to $2\pi/12$ h are broadly distributed around 180° E at latitudes poleward of 60° S,

11   which is consistent with the distribution of $\overline{KE}$ in Fig. 7. In this frequency range, the

12   energies of the gravity waves are very low near the center of Antarctica. Conversely, the

13   variances for frequencies from $2\pi/12$ h to $2\pi/6$ h are large over Antarctica and on the ice

14   sheet in the Ross Sea. These features suggest that the dynamical characteristics of the

15   gravity waves, such as the propagation paths, and/or the generation mechanisms may be

16   different in the two frequency ranges.

17

18   4.2.2. The meridional structure of the momentum flux spectra

19   Next, the frequency spectra of vertical fluxes of the zonal and meridional momentum

20   ($\mathrm{Re}[U(\omega)W^*(\omega)]$, $\mathrm{Re}[V(\omega)W^*(\omega)]$) were obtained via the Blackman–Tukey (1958)

21   method. In Fig. 11, Zonally averaged $\mathrm{Re}[U(\omega)W^*(\omega)]$ and $\mathrm{Re}[V(\omega)W^*(\omega)]$ without

22   diurnal and semi-diurnal migrating tides and semi-diurnal non-migrating tides with $s =$

23   1 are shown at heights of 70 km, 55 km, 40 km, and 25 km in JJA. Hereafter, these

24   components are denoted $\mathrm{Re}[U(\widetilde{\omega)W}^*(\omega)]$ and $\mathrm{Re}[V(\widetilde{\omega)W}^*(\omega)]$, respectively. Note

1   that the contributions of the tides to $\mathrm{Re}[U(\omega)W^*(\omega)]$ and $\mathrm{Re}[V(\omega)W^*(\omega)]$ are not

2   large in the mesosphere during the time period of JJA 2016 (not shown).

3   For $\mathrm{Re}[U(\omega)\widetilde{W^*}(\omega)]$, an isolated peak is observed near the inertial frequency from

4   55° S to 75° S at a height of 70 km. Another spectral peak at frequencies from $2\pi/10$ h to

5   $2\pi/8$ h from 77° S to 90° S appears to be similar to that of $\widetilde{P}_v(\omega)$ (Fig. 9). In addition,

6   large spectral values are distributed near 55° S at frequencies from $2\pi/12$ h to $2\pi/6$ h. The

7   signs of $\mathrm{Re}[U(\omega)\widetilde{W^*}(\omega)]$ are mostly negative over the entire frequency range. At

8   heights of 55 km and 40 km, there are large spectral values of $\mathrm{Re}[U(\omega)\widetilde{W^*}(\omega)]$ from

9   65° S to 75° S because the isolated peaks are distributed around the inertial frequency

10   from 55° S to 60° S but not from 65° S to 75° S. At a height of 25 km, two separated

11   spectral peaks are found at frequencies from $2\pi/24$ h to $2\pi/12$ h. One is centered from

12   45° S to 55° S, while the other is centered from 65° S to 80° S.

13   Conversely, the sign of $\mathrm{Re}[V(\omega)\widetilde{W^*}(\omega)]$ at a height of 25 km is negative from 45°

14   S to 55° S but positive from 65° S to 80° S. Under the assumption of upward propagation,

15   it is likely that gravity waves with large negative $\mathrm{Re}[U(\omega)\widetilde{W^*}(\omega)]$ at a height of 25 km

16   from 45° S to 55° S propagate poleward, while those from 65° S to 80° S propagate

17   equatorward. At heights of 40 km and 55 km, however, $\mathrm{Re}[V(\omega)\widetilde{W^*}(\omega)]$ around the

18   spectral peak of $\mathrm{Re}[U(\omega)\widetilde{W^*}(\omega)]$ at slightly lower frequencies than the inertial

19   frequency is mostly negative. These features suggest that the two spectral peaks at a

20   height of 25 km propagate toward 60° S and then merge into an isolated spectral peak at

21   a height of 40 km. At heights from 40 km to 70 km, gravity waves at frequencies lower

22   than the inertial frequencies from 60° S to 90° S have negative $\mathrm{Re}[V(\omega)\widetilde{W^*}(\omega)]$, while

23   those at frequencies higher than the inertial frequencies have positive $\mathrm{Re}[V(\omega)\widetilde{W^*}(\omega)]$.

24   From 30° S to 60° S, gravity waves at frequencies higher than the inertial frequencies have

1   negative $\mathrm{Re}[V(\omega)\widetilde{W}^*(\omega)]$.

2   To examine these features, the latitude–height sections of $\mathrm{Re}[\rho_0 U(\omega)\widetilde{W}^*(\omega)]$ and

3    $\mathrm{Re}[\rho_0 V(\omega)\widetilde{W}^*(\omega)]$ for gravity waves at frequencies from $2\pi/30$ h to $2\pi/12$ h are shown

4   in Fig. 12a, while those from $2\pi/12$ h to $2\pi/6$ h are shown in Fig. 12b. It is seen that

5    $\mathrm{Re}[\rho_0 U(\omega)\widetilde{W}^*(\omega)]$ both from $2\pi/30$ h to $2\pi/12$ h and from $2\pi/12$ h to $2\pi/6$ h has two

6   branches in the lower stratosphere, which merge southward of the polar night jet axis at

7   a height of approximately 40 km. The signs of $\mathrm{Re}[\rho_0 V(\omega)\widetilde{W}^*(\omega)]$ at frequencies from

8    $2\pi/30$ h to $2\pi/12$ h are positive (negative) at heights below 40 km along the low-latitude

9   (high-latitude) branch of $\mathrm{Re}[\rho_0 U(\omega)\widetilde{W}^*(\omega)]$, while they are primarily negative at

10   heights above 40 km. Conversely, the signs of $\mathrm{Re}[\rho_0 V(\omega)\widetilde{W}^*(\omega)]$ at frequencies from

11    $2\pi/12$ h to $2\pi/6$ h are positive (negative) poleward (equatorward) of 60° S from the lower

12   stratosphere to the mesosphere. These results indicate that gravity waves at frequencies

13   from $2\pi/12$ h to $2\pi/6$ h propagate into 60° S, which is similar to the previous picture of

14   the meridional propagation of gravity waves discussed by Sato et al. (2009). However,

15   gravity waves at frequencies from $2\pi/30$ h to $2\pi/12$ h propagate poleward above a height

16   of 40 km, not into the jet axis. This contrast is inherently related to the existence of the

17   isolated peaks around the inertial frequency at heights of 55–70 km in Fig. 11, which is

18   discussed in detail in Section 5. Note that $\mathrm{Re}[\rho_0 V(\omega)\widetilde{W}^*(\omega)]$ at frequencies from $2\pi/12$

19   h to $2\pi/6$ h has large negative values near a latitude of 30° S at heights above 35 km. This

20   may be related to the meridional propagation of convective gravity waves from the

21   equatorial region, as suggested by an observational study using MF radar (Yasui et al.,

22   2016).

23   A horizontal map of $\mathrm{Re}[U(\omega)\widetilde{W}^*(\omega)]$ at frequencies from $2\pi/30$ h to $2\pi/12$ h at a

24   height of 25 km is shown in Fig. 13a, while that at frequencies from $2\pi/12$ h to $2\pi/6$ h is

Atmospheric
Chemistry
and Physics
Discussions

1   shown in Fig. 13b. At latitudes from 65° S to 80° S, $\mathrm{Re}[U(\omega)\widetilde{W^*}(\omega)]$ has very large

2   negative values above the Antarctic Peninsula in both Figs. 13a and 13b. Negative values

3   of $\mathrm{Re}[U(\omega)\widetilde{W^*}(\omega)]$ are also found along the coast of Antarctica, in particular, above the

4   western side of the Ross Sea. Therefore, it is thought that the poleward branches of

5    $\mathrm{Re}[U(\omega)\widetilde{W^*}(\omega)]$ shown in Fig. 12 are primarily due to topographic gravity waves.

6   However, note that the gravity waves observed over the coast of Antarctica may be partly

7   due to non-orographic gravity waves caused by spontaneous radiation from the upper

8   tropospheric jet stream (Shibuya et al., 2016).

9   To examine the contribution of orographic/non-orographic gravity waves to the

10   equatorward branches in Fig. 12, the magnitudes of $\mathrm{Re}[U(\omega)\widetilde{W^*}(\omega)]$ from 42° S to 57°

11   S (the thick black circles in Fig. 13) were estimated over various topographies (the red

12   rectangles), islands (the green rectangles), and the Southern Ocean. The decomposition

13   of these domains is also described in Fig. 13. Over the latitudinal band from 42° S to 57°

14   S, the contributions of $\mathrm{Re}[U(\omega)\widetilde{W^*}(\omega)]$ due to gravity waves at frequencies from $2\pi/30$

15   h to $2\pi/12$ h over the topographies, islands, and Southern Ocean are 12.3%, 6.6%, and

16   81.1%, respectively, while those at frequencies from $2\pi/12$ h to $2\pi/6$ h are 7.1%, 6.0%,

17   and 86.9%, respectively. Therefore, the equatorward branch of $\mathrm{Re}[U(\omega)\widetilde{W^*}(\omega)]$ is

18   likely primarily composed of non-orographic gravity waves.

19   Finally, the horizontal scales of the wave disturbances contributing to

20   $\mathrm{Re}[U(\omega)\widetilde{W^*}(\omega)]$ were examined at each height. Hereafter, small-scale (large-scale)

21   wave disturbances are defined as components with horizontal wavelengths smaller than

22   (larger than) 1000 km, as occasionally defined in previous studies (e.g., Geller et al.,

23   2013). To extract the small-scale and large-scale components, a spatial filter was applied

24   to the wind data gridded in an x–y coordinate system centered at the South Pole as

25

Atmospheric
Chemistry
and Physics
Discussions

1   projected by the Lambert azimuthal equal-area projection. Figure 14 shows the zonally

2   averaged $\mathrm{Re}[\widetilde{U(\omega)W^*(\omega)}]$ resulting from large-scale and small-scale components

3   during JJA at heights of 70 km, 55 km, 40 km, and 25 km. At heights of 25 km and 40

4   km, it appears that the majority of $\mathrm{Re}[\widetilde{U(\omega)W^*(\omega)}]$ is composed of small-scale

5   components, while at heights of 55 km and 70 km, the large-scale components have large

6   negative values near the inertial frequencies. This feature is consistent with Shibuya et al.

7   (2017), who showed that mesospheric disturbances with large amplitude observed at

8   Syowa Station are due to quasi-12-hour gravity waves with horizontal wavelengths larger

9   than 1500 km. In addition, it appears that the spectral peak at frequencies from $2\pi/8$ h to

10   $2\pi/10$ h for the latitude range from 77° S to 90° S is also due to large-scale wave

11   disturbances.

12

13   **5. Discussion**

14   Recently, Sato et al. (2017) estimated the power spectra of horizontal and vertical

15   wind fluctuations and momentum flux spectra over a wide-frequency range from $2\pi/8$

16   min to $2\pi/20$ d using continuous PMSE observation data from the PANSY radar over

17   three summer seasons. It was shown that the spectral slope of $P_w(\omega)$ at frequencies from

18   $2\pi/2$ h to $2\pi/5$ d is nearly flat in the height range of 84–88 km, which is particularly clear

19   in the spectra of observations by the full PANSY system in the 2015–2016 summer season.

20   Even though the altitude range and season examined by Sato et al. (2017) are different

21   from those studied in this study, $P_w(\omega)$ simulated by NICAM, as shown in Fig. 8c, is

22   consistent with the PANSY radar observations. Moreover, Sato et al. (2017) demonstrated

23   that the power spectrum of the vertical flux of the zonal momentum ($\mathrm{Re}[U(\omega)W^*(\omega)]$)

24   has a positive isolated peak near the inertial frequency in the eastward background zonal

Atmospheric
Chemistry
and Physics
Discussions

1   wind in the summer season. The shape of $\mathrm{Re}[U(\omega)W^*(\omega)]$ shown in NICAM is

2   consistent with the results of Sato et al. (2017), even though the sign shown in this study

3   is negative under the westward background zonal wind in winter. Conversely, using the

4   Fe Boltzmann LIDAR at McMurdo Station (166.7° E 77.8° S), Chen et al. (2016) showed

5   that $P_{\mathrm{tem}}(\omega)$ has a broad spectrum peak at frequencies from $2\pi/3$ h to $2\pi/10$ h centered

6   at approximately $2\pi/8$ h at a height of 85 km in June for the five years of 2011–2015,

7   which is also consistent with the $P_{\mathrm{tem}}(\omega)$ result in Fig. 8d. The latitude–height section

8   of $\mathrm{Re}[\rho_0 V(\omega)\widetilde{W^*}(\omega)]$ in Fig. 12b indicates that the spectral peak from $2\pi/3$ h to $2\pi/10$

9   h is composed of gravity waves originating over the Antarctic continent. These results

10 indicate that the spectra of the mesospheric disturbances simulated in NICAM are very

11 realistic at high latitudes in the Southern Hemisphere.

12   The spectral peaks of $P_v(\omega)$ without the migrating tides in the mesosphere are

13 simulated near the inertial frequencies at latitudes from 30° S to 75° S. Therefore, the

14 quasi-12-hour inertia–gravity waves at Syowa Station examined by Shibuya et al. (2017)

15 can be interpreted as quasi-inertial period gravity waves. Moreover, it is shown that

16 $\mathrm{Re}[U(\omega)W^*(\omega)]$ also has negative isolated peaks near the inertial frequency. One

17 explanation for the existence of these isolated peaks can be derived from the propagation

18 characteristic of the gravity waves following Sato et al. (1999). The horizontal group

19 velocity C_{gh} and the vertical group velocity C_{gz} of the gravity waves are expressed as

$$C_{\mathrm{gh}} = \frac{2m^2(\hat{\omega}^2 - f^2)}{k(k^2 + m^2)}\frac{\vec{k}}{|k|} + \vec{U}, \qquad (7)$$

20   and

$$C_{\mathrm{gz}} = -\frac{2m(\hat{\omega}^2 - f^2)}{(k^2 + m^2)}. \qquad (8)$$

Atmospheric
Chemistry
and Physics
Discussions

1   It is easily confirmed from Eqs. (7) and (8) that C_{gh} and C_{gz} become zero when the

2   intrinsic frequency $\hat{\omega}$ is equal to the inertial frequency f at a latitude called the critical

3   latitude. When gravity waves propagate poleward and then reach the critical latitude, the

4   energies of the gravity waves may be accumulated with small C_{gh} and C_{gz} and be seen

5   as isolated peaks near the inertial frequency. Therefore, it is likely that the existence of

6   the clear isolated peaks near the inertial frequencies in the mesosphere is explained by the

7   poleward propagation of gravity waves with quasi-inertial frequencies and negative

8    $\mathrm{Re}[U(\omega)W^*(\omega)]$.

9   Moreover, the feature where the horizontal scales of the gravity waves become larger

10   near the inertial frequency in Fig. 14 is also explained by the accumulation of gravity

11   waves. Assuming that the explicit dependence of the absolute frequency function Ω on

12   x and t is contained entirely in the background wind $\vec{U}(x, t)$ and that the background

13   vertical wind velocity is negligible, the time evolution of the horizontal wavenumber

14   vector is described by

$$\frac{d_{\mathrm{g}}}{dt}\binom{k}{l} = -\begin{pmatrix} U_x & V_x \\ U_y & V_y \end{pmatrix}\binom{k}{l}, \tag{9}$$

15   where $\vec{U}$ denotes the background wind velocity, Ω is defined as $\Omega = \hat{\omega} + \vec{k} \cdot \vec{U}$, and

16   d_{g}/dt denotes the time derivative along the ray defined as $\partial/\partial t + \vec{C_{\mathrm{g}}} \cdot \vec{\nabla}$.

17   Here, the time evolution of the wave number is simplified by only considering the

18   meridional shear of the zonal background wind U_y:

$$\frac{d_{\mathrm{g}}}{dt}l = -U_y l. \tag{10}$$

19   Because the signs of $\mathrm{Re}[V(\omega)W^*(\omega)]$ for gravity waves with $\hat{\omega} \sim f$ are primarily

20   negative, the signs of l are also negative assuming upward propagation. In the high-

21   latitude region where $U_y > 0$ (Fig. 12), the absolute value of negative l becomes small,

Atmospheric
Chemistry
and Physics
Discussions

Open Access

EGU

1   indicating an increase in the horizontal wavelengths. Such a deformation is effective for

2   gravity waves with $\hat{\omega} \sim f$ due to their small C_{gh} and C_{gz}. This is likely the reason why

3   large-scale gravity waves contribute to the spectral peaks of $\mathrm{Re}[U(\omega)W^*(\omega)]$ near the

4   inertial frequencies primarily in the mesosphere. In addition, the deformation may also

5   contribute to small $\mathrm{Re}[V(\omega)\widetilde{W^*}(\omega)]$ around f in the mesosphere (Fig. 11) owing to

6   small negative l.

7   Note that the intrinsic frequency is not equal to the observed frequency owing to the

8   Doppler shift:

$$\hat{\omega} = \omega - \vec{U} \cdot \vec{k}. \tag{9}$$

9   It was shown that $\mathrm{Re}[U(\omega)W^*(\omega)]$ has negative spectral values at heights from 25 km

10   to 70 km in the winter high-latitude Southern Hemisphere. This indicates that gravity

11   waves have negative zonal wavenumbers in the westerly jet. Therefore, the intrinsic

12   frequency should be larger than the observed frequency in Eq. (9), suggesting that the

13   poleward propagation of gravity waves with low frequency stops poleward of a latitude

14   where $\omega \sim f$ in the Southern Hemisphere. This is likely the reason why the isolated

15   peaks near the inertial frequency in Figs. 9 and 11 exist at frequencies slightly smaller

16   than the inertial frequency. This hypothesis is supported by the fact that the signs of

17   $\mathrm{Re}[V(\omega)W^*(\omega)]$ at frequencies slightly longer than the inertial frequency are negative.

18   However, further studies are required to understand the existence of the isolated

19   peaks in the mesosphere. At a height of 25 km, gravity waves with large negative

20   $\mathrm{Re}[U(\omega)W^*(\omega)]$ tend to prefer frequencies from $2\pi/12$ h to $2\pi/24$ h, which is related

21   to the existence of the isolated peaks in the mesosphere. The physical reasons why these

22   observed frequencies are preferred are still unclear. Moreover, the signs of

Atmospheric
Chemistry
and Physics
Discussions

Open Access

EGU

1 $\mathrm{Re}[V(\omega)W(\omega)]$ at the isolated peaks from $2\pi/8$ h to $2\pi/10$ h from $77°$ S to $90°$ S are

2 positive throughout the middle atmosphere, suggesting that these peaks are due to gravity

3 waves originating from a region over the Antarctic continent and/or the coastal region

4 and not from low-latitude regions. These points should be examined relative to the

5 generation mechanisms of gravity waves, which are related to the observed frequencies

6 of the gravity waves.

7   It appears that the quasi-12-hour gravity waves have horizontal scales larger than at

8 least 1000 km. Such gravity waves are not fully resolved by the MERRA reanalysis data

9 (Fig. 5), likely because the vertical resolution of MERRA ($\Delta z \sim 3.2$ km) is insufficient

10 to simulate gravity waves with such vertical wavelengths. The momentum deposition

11 caused by the quasi-inertial-period gravity waves may not be calculated by

12 parameterizations because current parameterization schemes focus only on gravity waves

13 with short horizontal wavelengths. The momentum deposition missed from such quasi-

14 inertia–gravity waves may be one of the key components needed to solve the cold-bias

15 problem in the winter–spring polar middle atmosphere.

16

17 **6. Summary**

18   The first long-term simulation using the high-top non-hydrostatic general circulation

19 model was performed to analyze mesospheric gravity waves in the period from April to

20 August 2016. Successive runs lasting 7 days were run using initial conditions from the

21 MERRA reanalysis data with a two-day overlap between consecutive runs. The data for

22 the analyses were compiled using the final 5 d of each simulation. The analysis was

23 carefully performed to avoid the influence of artificial gaps between the different runs.

24 Our main results are summarized as follows.

Atmospheric
Chemistry
and Physics

Open Access

EGU

Discussions

1 ● The mesospheric wind fields simulated by NICAM are realistic according to a

2   comparison with the PANSY radar observations, even though the amplitudes of the

3   wind disturbances appear to be larger than those of the observations. The large-scale

4   structure of the zonally averaged zonal winds in the latitude–height section is also

5   comparable to the features in the MERRA reanalysis data.

6 ● Power spectra of the u and v fluctuations at Syowa Station have an isolated peak

7   at the frequency of $2\pi/12$ h and obey a power law with an exponent of approximately

8     $-5/3$ in the frequency region higher than the inertial frequency f (corresponding to

9     $2\pi/12.7$ h), while that of w has a flat structure (i.e., $\propto \omega^0$) at frequencies from $2\pi/2$

10   h to $2\pi/5$ d. The power spectrum of the v fluctuations without the migrating and

11   non-migrating tides has isolated peaks at frequencies slightly lower than f at

12   latitudes from 30° S to 75° S, while it has isolated peaks at frequencies of

13   approximately $2\pi/8$ h at latitudes from 78° S to 90° S.

14 ● The spectrum of the vertical fluxes of the zonal momentum also has isolated peaks

15   at frequencies slightly lower than f at latitudes from 30° S to 75° S at a height of

16   70 km. The isolated peaks are primarily due to gravity waves with horizontal

17   wavelengths of more than 1000 km. The latitude–height structure of the momentum

18   fluxes indicates that the isolated peaks at frequencies slightly lower than f originate

19   from two branches of gravity wave propagation. It is thought that one of the branches,

20   originating from 75° S, is composed of topographic gravity waves generated over the

21   Antarctic Peninsula and its coast, while more than 80% of the other, originating from

22   45° S, is composed of non-orographic gravity waves.

23 ● It is suggested that the physical explanation for the existence of the isolated peaks in

24   the high-latitude region in the mesosphere is related to the poleward propagation of

Atmospheric
Chemistry
and Physics
Discussions

1   quasi-inertial frequency gravity waves and the accumulation of wave energies near

2   their inertial frequencies with very small group velocities.

3

4   This study offers a quantitative discussion based on high-resolution observations and

5   numerical models. Statistical analyses of inertia–gravity waves in the mesosphere in

6   different seasons are required to understand the momentum budget in the mesosphere

7   combining the PANSY observations and numerical simulations using NICAM.

8

9

10 **7. Data availability**

11 The PANSY radar observation data is available at the project website, http://pansy.eps.s.u-

12 tokyo.ac.jp. Model outputs are available on request from the corresponding author.

13

14 **8. Competing interest**

15 The authors declare that they have no conflict of interest.

16

17   **Acknowledgements**

Atmospheric
Chemistry
and Physics
Discussions

Open Access

EGU

10

11

Atmospheric
Chemistry
and Physics
Discussions

1

References

3 Alexander, M. J., and Barnet, C.: Using satellite observations to constrain

4   parameterizations of gravity wave effects for global models, J. Atmos. Sci., 64,

5   1652-1665, 2007

6 Alexander, M. J. and H, Teitelbaum.: Observation and analysis of a large amplitude

7   mountain wave event over the Antarctic peninsula. Journal of Geophysical

8   Research: Atmospheres, 112(D21), 2007

9 Alexander, M. J., Geller, M., McLandress, C., Polavarapu, S., Preusse, P., Sassi, F.,

10   Sato, K., Eckermann, S., Ern, M., Hertzog, A., Kawatani, Y., Pulido, M., Shaw, T.,

11   Sigmond, M., Vincent, R., and Watanabe, S.: Recent developments in gravity wave

12   effects in climate models, and the global distribution of gravity wave momentum

13   flux from observations and models, Q. J. Roy. Meteorol. Soc., 136, 1103-1124,

14   2010

15 Arnold, K. S., and She, C. Y.: Metal fluorescence lidar (light detection and ranging) and

16   the middle atmosphere. Contemporary Physics, 44(1), 35-49, 2003

17 Aso, T.: A note on the semidiurnal non-migrating tide at polar latitudes, Earth Planets

18   Space, 59, e21–e24, 2007

19 Baumgaertner, A. J. G., McDonald, A. J., Hibbins, R. E. , Fritts, D. C., Murphy, D. J.,

20   and Vincent, R. A.: Short-period planetary waves in the Antarctic middle

21   atmosphere, J. Atmos. Sol. Terr. Phys., 70(10), 1336–1350,

22   doi:10.1016/j.jastp.2008.04.007, 2008

23 Becker, E., 2009: Sensitivity of the upper mesosphere to the Lorenz energy cycle of the

24   troposphere, J. Atmos. Sci., 66, 647–666, doi: 10.1175/2008JAS2735.1.

Atmospheric
Chemistry
and Physics
Discussions

Open Access

EGU

1 Beres, J. H., Alexander, M. J. and Holton, J. R.: A method of specifying the gravity

2   wave spectrum above convection based on latent heating properties and

3   background wind. Journal of the atmospheric sciences, 61(3), 324-337, 2004

4 Blackman, R. B., and Tukey, J. W.: The Measurement of Power Spectra from the Point

5   of View of Communications Engineering, Dover,New York, 1958

6 Bloom, S., Takacs, L., DaSilva, A., and Ledvina, D.: Data assimilation using

7   incremental analysis updates. Mon. Wea. Rev., 124, 1256–1271, 1996.

8 Cámara, A., Lott, F. and Hertzog, A.: Intermittency in a stochastic parameterization of

9   nonorographic gravity waves. Journal of Geophysical Research:

10   Atmospheres, 119(21), 2014

11 Charron, M. and Manzini, E.: Gravity waves from fronts: Parameterization and middle

12   atmosphere response in a general circulation model. Journal of the atmospheric

13   sciences, 59(5), 923-941, 2002

14 Chen, C., Chu, X., McDonald, A. J., Vadas, S. L., Yu, Z., Fong, W., and Lu, X.:

15   Inertia‐gravity waves in Antarctica: A case study using simultaneous lidar and

16   radar measurements at McMurdo/Scott Base (77.8° S, 166.7° E). Journal of

17   Geophysical Research: Atmospheres, 118(7), 2794-2808, 2013.

37 Chen, C., Chu, X., Zhao, J., Roberts, B. R., Yu, Z., Fong, W., Lu, X., and Smith J. A.:

38   Lidar observations of persistent gravity waves with   periods of 3–10 h in the

39   Antarctic middle and upper atmosphere at McMurdo (77.83∘S, 166.67∘E), J.

40   Geophys. Res. Space Physics, 121,1483–1502, doi:10.1002/2015JA022127, 2016.

41 Dowdy, A. J., Vincent, R. A., Tsutsumi, M., Igarashi, K., Murayama, Y., Singer, W., and

42   Murphy, D. J.: Polar mesosphere and lower thermosphere dynamics: 1. Mean wind

43   and gravity wave climatologies, J. Geophys. Res., 112, D17104,

Atmospheric
Chemistry
and Physics
Discussions

1   doi:10.1029/2006JD008126, 2007

2   Eckermann, S. D., and Preusse, P.: Global measurements of stratospheric mountain

3   waves from space, Science, 286, 1534–1537, 1999.

4   Ern, M., Preusse, P., Gille, J. C., Hepplewhite, C. L., Mlynczak, M. G., Russell III, J.

5   M., and Riese, M.: Implications for atmospheric dynamics derived from global

6   observations of gravity wave momentum flux in stratosphere and mesosphere. J.

7   Geophys. Res., 116, D19107, doi:10.1029/2011JD015821, 2011

8   Eyring, V., Shepherd, T. G., and Waugh, D. W.: SPARC CCMVal report on the

9   evaluation of chemistry-climate models. SPARC Rep., 5, WCRP-132, WMO/TD-

10   No. 1526, 434 pp, Eds., 2010.

11   Forbes, J. M., Makarov, N. A., and Portnyagin, Y. I.: First results from the meteor radar

12   at south pole: A large 12-hour oscillation with zonal wavenumber one, Geophys.

13   Res. Lett., 22, 3247– 3250, 1995

14   Fritts, D. C., and Vincent, R. A.: Mesospheric momentum flux studies at Adelaide,

15   Australia: Observations and a gravity wave–tidal interaction model. Journal of the

16   Atmospheric Sciences, 44(3), 605-619, 1987.

17   Fritts, D. C.: Errant inferences of gravity wave momentum and heat fluxes using

18   airglow and lidar instrumentation: Corrections and cautions. Journal of

19   Geophysical Research: Atmospheres, 105(D17), 22355-22360, 2000.

20   Fritts , D. C. and Alexander, M. J.: Gravity wave dynamics and effects in the middle

21   atmosphere. Rev. Geophys., 41, 1003, doi:10.1029/2001RG000106, 2003.

22   Fritts and Coauthors: The Deep Propagating Gravity Wave Experiment (DEEPWAVE):

23   An airborne and ground-based exploration of gravity wave propagation and effects

24   from their sources throughout the lower and middle atmosphere. Bull. Amer.

1   Meteor. Soc., doi:10.1175, 97(3), 425-453, doi:10.1175/BAMS-D-14-00269.1,

2   2016

3   Garcia, F. J., Kelley, M. C., Makela, J. J., and Huang, C.-S.: Airglow observations of

4   mesoscale low-velocity traveling ionospheric disturbances at midlatitudes, J.

5   Geophys. Res., 105(A8), 18407–18415, doi:10.1029/1999JA000305, 2000.

6   Gardner, C. S., Kane, T. J., Senft, D. C., Qian, J., and   Papen, G. C.: Simultaneous

7   observations of sporadic E, Na, Fe, and Ca^+ layers at Urbana, Illinois: Three case

8   studies, J. Geophys. Res., 98(D9), 16865–16873, doi:10.1029/93JD01477, 1993.

9   Geller, M. A., Alexander, M., Love, P. T., Bacmeister, J., Ern, M., Hertzog, A., and

10   Zhou, T.: A Comparison between Gravity Wave Momentum Fluxes in Observations

11   and Climate Models. Journal of Climate, 26(17), 2013.

12   Hertzog, A., Boccara, G., Vincent, R. A., Vial, F., and Cocquerez, P.: Estimation of

13   gravity wave momentum flux and phase speeds from quasi-Lagrangian

14   stratospheric balloon flights. Part II: Results from the Vorcore campaign in

15   Antarctica. Journal of the Atmospheric Sciences, 65(10), 3056-3070, 2008.

16   Hibbins, R. E., Marsh, O. J., McDonald, A. J., and Jarvis, M. J.: A new perspective on

17   the longitudinal variability of the semidiurnal tide, Geophys. Res. Lett., 37,

18   L14804, doi:10.1029/2010GL044015, 2010.

19   Hibbins, R.E., Espy, P.J., Jarvis, M.J., Riggin, D.M., Fritts, D.C.: A climatology of tides

20   and gravity wave variance in the MLT above Rothera, Antarctica obtained by

21   MFradar. J. Atmos. Solar-Terr. Phys. 69 (4–5), 578–588, 2007.

22   Hindley, N. P., Wright, C. J., Smith, N. D. and Mitchell, N. J.: The southern

23   stratospheric gravity wave hot spot: individual waves and their momentum fluxes

24   measured by COSMIC GPS-RO. Atmospheric Chemistry and Physics, 15(14),

Atmospheric
Chemistry
and Physics
Discussions
Open Access
EGU

1   7797-7818, 2015.

18   Hoffmann, P., Becker, E., Singer, W., and Placke, M., : Seasonal variation of

19   mesospheric waves at northern middle and high latitudes, J. Atmos. Sol. Terr.

20   Phys., 72(14–15), 1068–1079, doi:10.1016/j.jastp.2010.07.002, 2010.

21   Hoffmann, L., Xue, X., and Alexander, M. J.: A global view of stratospheric gravity

22   wave hotspots located with Atmospheric Infrared Sounder observations, J.

23   Geophys. Res.-Atmos., 118, 416–434, doi:10.1029/2012JD018658, 2013.

24   Jiang, J. H., Eckermann, S. D., Wu, D. L., Hocke, K., Wang, B., Ma, J., and Zhang, Y.:

25   Seasonal variation of gravity wave sources from satellite observation. Advances in

26   Space Research, 35(11), 1925-1932, 2005.

27   Jewtoukoff, V., Hertzog, A., Plougonven, R.. de la Cámara, A.. and Lott, F.: Comparison

28   of gravity waves in the Southern Hemisphere derived from balloon observations

29   and the ECMWF analyses. J. Atmos. Sci., 72, 3449–2468, doi:10.1175/ JAS-D-14-

30   0324.1, 2015.

31   Kovalam, S., and Vincent, R. A.: Intradiurnal wind variations in the midlatitude and

32   high-latitude mesosphere and lower thermosphere, J. Geophys. Res., 108, 4135,

33   doi:10.1029/2002JD002500, D4, 2003.

34   Liu, H. L., McInerney, J. M., Santos, S., Lauritzen, P. H., Taylor, M. A., and Pedatella,

35   N. M.: Gravity waves simulated by high‐resolution Whole Atmosphere

36   Community Climate Model. Geophysical Research Letters, 41(24), 9106-9112,

37   2014.

38   Matsuda, T. S., Nakamura, T., Ejiri, M. K., Tsutsumi, M., and Shiokawa, K.: New

39   statistical analysis of the horizontal phase velocity distribution of gravity waves

40   observed by airglow imaging, J. Geophys. Res. Atmos., 119, 9707–9718,

Atmospheric
Chemistry
and Physics
Discussions

1   doi:10.1002/2014JD021543, 2014.

2   McFarlane, N. A.: The effect of orographically excited gravity wave drag on the general

3   circulation of the lower stratosphere and troposphere. Journal of the atmospheric

4   sciences, 44(14), 1775-1800, 1987.

5   Muraoka, Y., Fukao, S., Sugiyama, T., Yamamoto, M., Nakamura, T., Tsuda, T., and

6   Kato, S.: Frequency-spectra of mesospheric wind fluctuations observed with the

7   MU radar, Geophys. Res. Lett., 17(11), 1897–1900,

8   doi:10.1029/Gl017i011p01897, 1990.

9   Murphy, D. J., et al.: A climatology of tides in the Antarctic mesosphere and lower

10   thermosphere, J. Geophys. Res., 111, doi:10.1029/2005JD006803, 2006.

11 Murphy, D.J., French, W.J.R., Vincent, R.A.: Long-Period Planetary Waves in the

12   mesosphere and lower thermosphere above Davis, Antarctica. Journal of

13   Atmospheric and Solar-Terrestrial Physics, doi:10.1016/j.jastp.2007.06.008, 2007.

14 Murphy, D. J., Aso, T., Fritts, D. C., Hibbins, R. E., McDonald, A. J., Riggin, D. M.,

15   Tsutsumi, M., and Vincent, R. A.: Source regions for Antarctic MLT non-

16   migrating semidiurnal tides, Geophys. Res. Lett., 36, L09805,

17   doi:10.1029/2008GL037064, 2009.

18 Nicolls, M. J., Varney, R. H., Vadas, S. L., Stamus, P. A., Heinselman, C. J., Cosgrove,

19   R. B., and Kelley, M. C.: Influence of an inertia-gravity wave on mesospheric

20   dynamics: A case study with the Poker Flat Incoherent Scatter Radar, J. Geophys.

21   Res., 115, D00N02, doi:10.1029/2010JD014042, 2010.

22 Nishiyama, T., Sato, K., Nakamura, T., Tsutsumi, M., Sato, T., Kohma, M., Nishimura,

23   K., Tomikawa, Y., Ejiri, M. K., and Tsuda, T. T.: Height and time characteristics of

24   seasonal and diurnal variations in PMWE based on 1 year observations by the

Atmospheric
Chemistry
and Physics
Discussions

Open Access

1   PANSY radar (69.0°S, 39.6°E), Geophys. Res. Lett., 42, 2100-2108. doi:

2   10.1002/2015GL063349, 2015.

3   Nozawa, T., Nagashima, T., Ogura, T., Yokohata, T., Okada, N., and Shiogama, H.:

4   Climate change simulations with a coupled ocean-atmosphere GCM called the

5   Model for Interdisciplinary Research on Climate: MIROC, CGER Supercomput.

6   Monogr. Rep., 12, Cent. For Global Environ. Res., Natl. Inst. for Environ. Stud.,

7   Tsukuba, Japan, 2007.

8   Plougonven, R., Hertzog A., and Guez, L.: Gravity waves over Antarctica and the

9   Southern Ocean: consistent momentum fluxes in mesoscale simulations and

10   stratospheric balloon observations. Quarterly J. Roy. Meteor. Soc., 139, 101-118,

11   2013.

12   Preusse, P., Schaeler, B., Bacmeister, J. T., & Offermann, D.: Evidence for gravity

13   waves in CRISTA temperatures. Advances in Space Research, 24(11), 1601-1604,

14   1999.

15   Preusse, P., Eckermann, S. D., Ern, M., Oberheide, J., Picard, R. H., Roble, R. G.,

16   Riese, M., Russell, III, J. M., and Mlynczak, M. G.: Global ray tracing simulations

17   of the SABER gravity wave climatology, J. Geophys. Res., 114, D08126,

18   doi:10.1029/2008JD011214, 2009.

19   Rabier, F., Bouchard, A., Brun, E., Doerenbecher, A., Guedj, S., Guidard, V., Karbou, F.,

20   Peuch, V-H., Amraoui, L. El., Puech, D., Genthon, C., Picard, G., Town, M.,

21   Hertzog, A., Vial, F., Cocquerez, P., Cohn, S. A., Hock, T., J. Fox, H. Cole, D.

22   Parsons, J. Powers,   K. Romberg, J. Van An del, T. Deshler, J. Mercer, J. S. Haase,

23   L. Avallone, L. Kalnajs, C. R. Mechoso, A. Tangborn, A. Pellegrini, Y. Frenot, J-N.

24   Thepaut, A. P. McNally, G. Balsamo, Steinle, P.: The Concordiasi project in

1   Antarctica. Bull. American Meteorol. Soc. 91: 69–86, 2010.

105 Reid, I. M., and Vincent, R. A.: Measurements ofmesospheric gravity wave momentum

106   fluxes and mean flow accelerations at Adelaide, Australia, J. Atmos. Terrest. Phys.

107   49, 443-460, 1987.

108 Richter, J. H., Sassi, F., and Garcia, R. R.: Toward a physically based gravity wave

109   source parameterization in a general circulation model, J. Atmos. Sci., 67, 136–

110   156, 2010.

111 Rienecker, M., and Coauthors: MERRA: NASA's ModernEra Retrospective Analysis

112   for Research and Applications. J. Climate, 24, 3648–3624, 2011.

113 Sato, K: Vertical wind disturbances in the troposphere and lower stratosphere observed

114   by the MU radar, J. Atmos. Sci., 47, 2803-2817, 1990.

115 Sato, K., Tsutsumi, M., Sato, T., Nakamura, T., Saito, A., Tomikawa, Y., Nishimura, K.,

116   Kohma, M., Yamagishi, H., and Yamanouchi, T.: Program of the Antarctic Syowa

117   MST/IS Radar (PANSY), J. Atmos. Solar-Terr. Phys., 118A, 2-15, 2014.

118 Sato, K., Watanabe, S., Kawatani, Y., Tomikawa, Y., Miyazaki, K., and Takahashi,

119   M.: On the origins of mesospheric gravity waves, Geophys. Res. Lett., 36, L19801,

120   doi:10.1029/2009GL039908, 2009.

121 Sato, K., Kumakura, T., and Takahashi, M.: Gravity waves appearing in a high-

122   resolution GCM simulation, J. Atmos. Sci., 56, No.8, 1005-1018, 1999.

123 Sato, K., Tateno S., Watanabe, S., and Kawatani, Y.: Gravity wave characteristics in the

124   Southern Hemisphere revealed by a high-resolution middle-atmosphere general

125   circulation model. J. Atmos. Sci., 69, 1378–1396, doi:10.1175/JAS-D-11-0101.1,

126   2012.

127 Sato, K., and Yoshiki, M.: Gravity wave generation around the polar vortex in the

Atmospheric
Chemistry
and Physics
Discussions

1   stratosphere revealed y 3-houly radiosonde observations at Syowa Station. J.

2   Atmos. Sci., 65, 3719-3735, 2008.

3   Sato, K., Kohma, M., Tsutsumi, M., and Sato, T.: Frequency spectra and vertical profiles

4   of wind fluctuations in the summer Antarctic mesosphere revealed by MST radar

5   observations. Journal of Geophysical Research: Atmospheres 122:1, 3-19, 2017.

6   Satoh, M., Matsuno, T., Tomita, H., Miura, H., Nasuno, T., and Iga, S.: Nonhydrostatic

7   icosahedral atmospheric model (NICAM) for global cloud resolving simulations. J.

8   Comput. Phys., the special issue of Predicting Weather, Climate and Extreme

9   Events, 227, 3486−3514, doi: 10.1016/j.jcp.2007.02.006, 2008.

10   Satoh, M., Tomita, H., Yashiro, H., Miura, H., Kodama, C., Seiki, T., Noda, A. T.,

11   Yamada, Y., Goto, D., Sawada, M., Miyoshi, T., Niwa, Y., Hara, M., Ohno, T., Iga,

12   S., Arakawa, T., Inoue, T., Kubokawa, H.: The Non-hydrostatic Icosahedral

13   Atmospheric Model: Description and Development. Progress in Earth and

14   Planetary Science, 1, 18. doi:10.1186/s40645-014-0018-1, 2014.

15   Scinocca, J. F.: An accurate spectral nonorographic gravity wave drag parameterization

16   for general circulation models. J. Atmos. Sci., 60, 667-682, 2003.

17   Shibuya R., Miura, H., and Sato, K.: A grid transformation method for a quasi-uniform,

18   circular fine region using the spring dynamic, Journal of the Meteorological

19   Society of Japan, 94, doi:10.2151/jmsj.2016-022, 2016.

20   Shibuya, R., K. Sato, Y. Tomikawa, M. Tsutsumi and T. Sato, 2015: A study of multiple

21   tropopause structures caused by inertia-gravity waves in the Antarctica, J. Atmos.

22   Sci., 72, 2109–2130.

23   Shibuya, R., Sato, K., Tsutsumi, M., Sato, T., Tomikawa, Y., Nishimura, K., and Kohma,

24   M.: Quasi-12h inertia-gravity waves in the lower mesosphere observed by the

Atmospheric
Chemistry
and Physics
Discussions

1   PANSY radar at Syowa Station (39.6 °E ,69.0 °S), Atmos. Chem. Phys., 17, 6455-

2   6476, doi:10.5194/acp-17-6455-2017, 2017.

3   Song, I. S. and Chun, H. Y.: Momentum flux spectrum of convectively forced internal

4   gravity waves and its application to gravity wave drag parameterization. Part I:

5   Theory. Journal of the atmospheric sciences, 62(1), 107-124, 2005.

6   Talaat, E. R., and Mayr, H.G.: Model of semidiurnal pseudo tide in the high-latitude

7   upper mesosphere, Journal of Atmospheric and Solar-Terrestrial Physics, 73, 2386–

8   2391, 2011.

9   Tomikawa, Y., Sato, K., Watanabe, S., Kawatani, Y., Miyazaki, K., and Takahashi, M.:

10   Growth of planetary waves and the formation of an elevated stratopause after a

11   major stratospheric sudden warming in a T213L256 GCM, J. Geophys.

12   Res.,117, D16101, doi:10.1029/2011JD017243, 2012.

13   Tomita, H., Satoh, M., and Goto, K.: An optimization of icosahedral grid by using

14   spring dynamics. J. Comp. Phys., 183, 307-331, 2002.

15   Tsutsumi, M., Tsuda, T., Nakamura, T., and Fukao, S.: Temperature fluctuations near

16   the mesopause inferred from meteor observations with the middle and upper

17   atmosphere radar, Radio Sci., 29(3), 599–610, doi:10.1029/93RS03590, 1994.

18   Vincent, R. A., and Fritts, D. C.: A climatology of gravity wave motions in the

19   mesopause region at Adelaide, Australia. Journal of the atmospheric

20   sciences, 44(4), 748-760, 1987.

35   Watanabe, S., and Miyahara, S.: Quantification of the gravity wave forcing of the

36   migrating diurnal tide in a gravity wave-resolving general circulation model. J.

37   Geophys. Res. 114: D07110. DOI:10.1029/2008JD011218, 2009.

38   Watanabe, S., Kawatani, Y., Tomikawa, Y., Miyazaki, K., Takahashi, M., and Sato, K.:

39   General Aspects of a T213L256 Middle Atmosphere General Circulation Model, J.

1   Geophys. Res., 113, D12110, doi:10.1029/2008JD010026, 2008.

2 Watanabe, S., Sato, K., Kawatani, Y., and Takahashi, M.: Vertical resolution dependence

3   of gravity wave momentum flux simulated by an atmospheric general circulation

4   model, Geosci. Model Dev., 8, 1637-1644, doi:10.5194/gmd-8-1637-2015, 2015.

5 Wu, D. L. and Waters, J. W.: Satellite observations of atmospheric variances: A possible

6   indication of gravity waves. Geophysical Research Letters, 23(24), 3631-3634,

7   1996.

8 Wu, W.-S., Purser, R. J., and Parrish, D. F.: Three-dimensional variational analysis with

9   spatially inhomogeneous covariances. Mon. Wea. Rev., 130, 2905–2916, 2002.

10 Wu, D. L., Preusse, P., Eckermann, S. D., Jiang, J. H., de la Torre Juarez, M., Coy, L.

11   and Wang, D. Y.: Remote sounding of atmospheric gravity waves with satellite

12   limb and nadir techniques, Advances in Space Research, 37(12), 2269-2277, 2006.

13 Yamashita, C., England, S. L., Immel, T. J., & Chang, L. C.: Gravity wave variations

14   during elevated stratopause events using SABER observations. Journal of

15   Geophysical Research: Atmospheres, 118(11), 5287-5303, 2013.

16 Yasui, R., Sato, K., and Tsutsumi, M.: Seasonal and interannual variation of

17   mesospheric gravity waves based on MF radar observations over 15 years at

18   Syowa Station in the Antarctic., SOLA, 12, 46-50, doi:10.2151/sola.2016-010,

19   2016.

20 Yoshiki, M., and Sato, K.:A statistical study of gravity waves in the polar regions based

21   on operational radiosonde data, J. Geophys. Res., 105(D14), 17,995–18,011, 2000.

22 Zülicke, C., and Becker, E.: The structure of the mesosphere during sudden

23   stratospheric warmings in a global circulation model, J. Geophys. Res. Atmos.,

24   118, 2255–2271, doi:10.1002/jgrd.50219, 2013.

Atmospheric
Chemistry
and Physics
Discussions

Table 1:   Physics scheme used in the high-top NICAM

Physics	Description
Cloud Microphysics	NICAM Single-moment Water 6 (NSW6) (Tomita 2008)
Cumulus Convection	Not used
Radiation	MstrnX (Sekiguchi and Nakajima, 2008)
Turbulence	Meller-Yamada Nakanishi-Niino (MYNN2) (Nakanishi and Niino, 2006)
Gravity wave	Not used
Land surface	Minimal Advanced Treatments of Surface Interaction and RunOff (MATSIRO) (Takata et al., 2003)
Surface flux (ocean)	Bulk surface flux by Louis (1979)
Ocean model	Single layer slab-ocean

1

2

Atmospheric
Chemistry
and Physics
Discussions
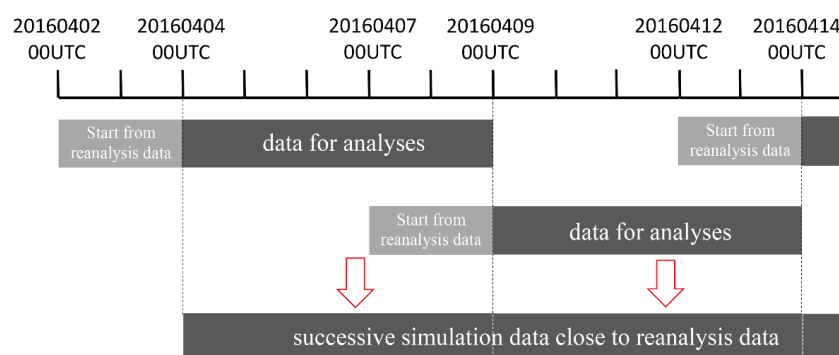
1 **Figures**

Figure 1: An illustration for the time integration method.

2

3

Atmospheric
Chemistry
and Physics
Discussions

Open Access
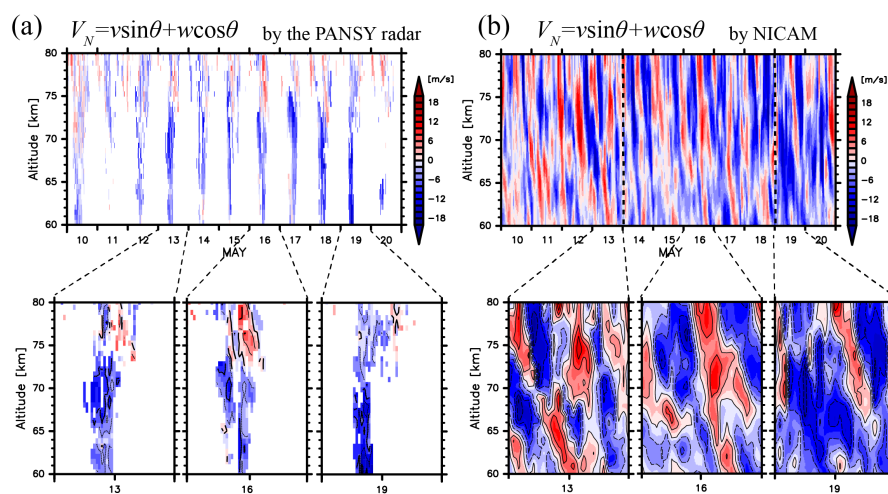
Figure 2: Time-altitude cross sections of northward line of sight speeds (a) observed by the PANSY radar at Syowa Station (a) for the period from 10 to 20 May 2015, and (b) those simulated by NICAM in the same period. The contour intervals are 4 m s^{-1}. The black dotted vertical lines in (b) denotes the segments of the lasting five-day-simulation.

1

2

Atmospheric
Chemistry
and Physics
Discussions

Open Access

EGU
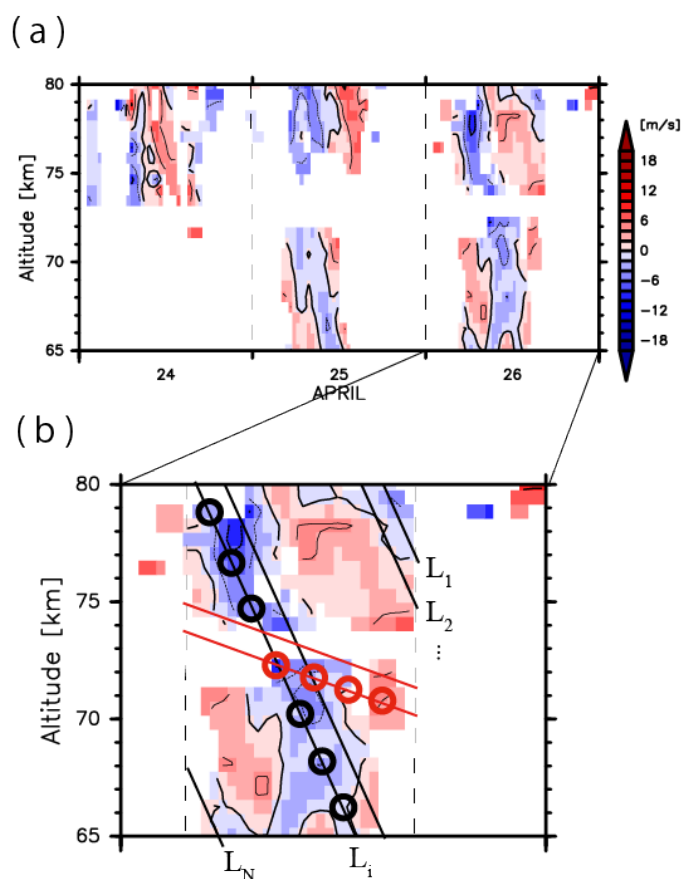
Figure 3: Time-altitude cross sections of northward line of sight speeds (a) observed by the PANSY radar for the period from (a) 24 to 26 April 2016 and (b) 26 April 2016. (b) Phase lines with a vertical phase velocity of V_1 are denoted as L_1, L_2, …, L_i, …L_N (thick black lines), and data points on L_i are denoted as x_1^i, x_2^i, …, $x_{n_i}^i$ (black circles). Another phase lines with a vertical phase velocity of V_2 and data points on their phase lines are depicted by a red color. Please see the text in detail.

1

2
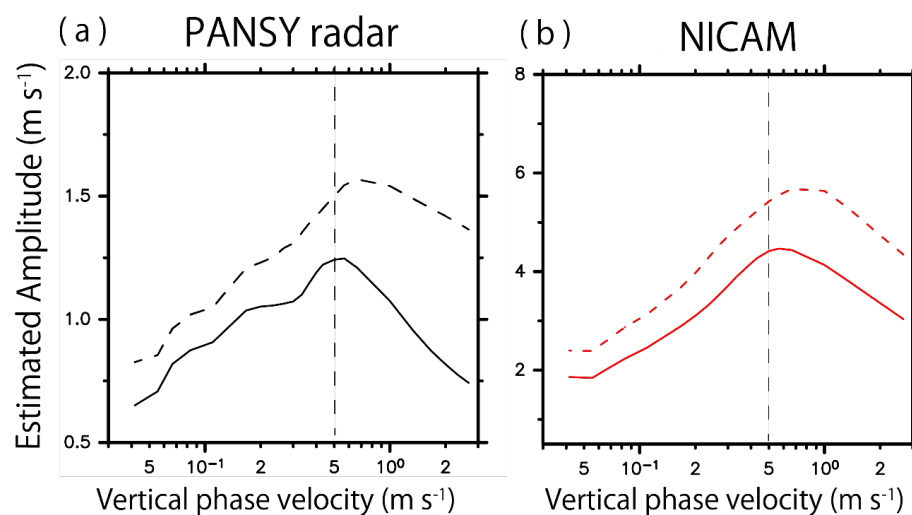
Figure 4: Estimated wave amplitude as a function of vertical phase velocities in April (black curves) and in May (dashed curves) using (a) the PANSY radar observation and (b) the NICAM simulation.

1

2
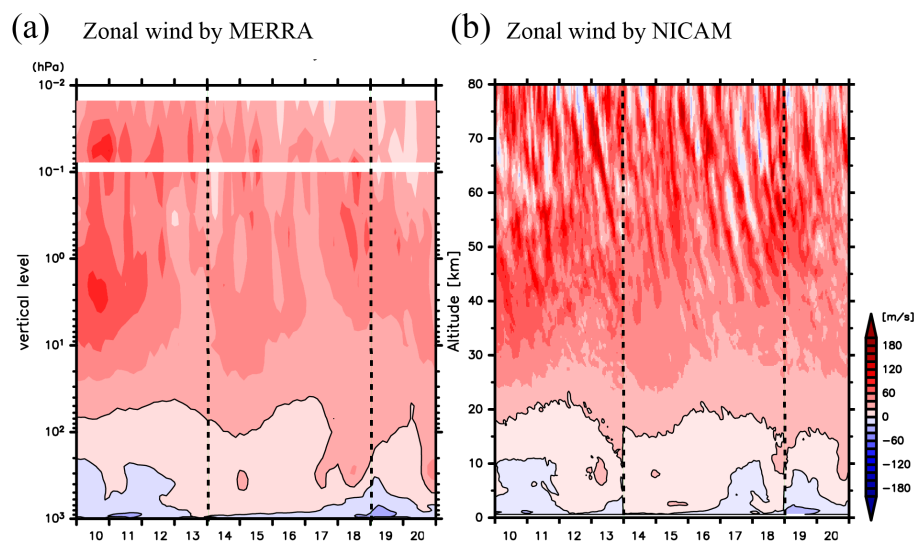
Figure 5: Time-altitude cross sections of zonal winds (a) from the MERRA reanalysis data and (b) from NICAM simulations for the period from May 10 to May 20 2015 at a grid near Syowa Station. The contour intervals are 20 m s^{-1}. The vertical dotted lines denotes the segments of the continuous five-day-simulation by NICAM. (a) The 3-D assimilated fields of the MERRA reanalysis data for 1000 hPa to 0.1 hPa and the 3-D analyzed fields for 0.1 hPa to 0.01 hPa are drawn.

1

2
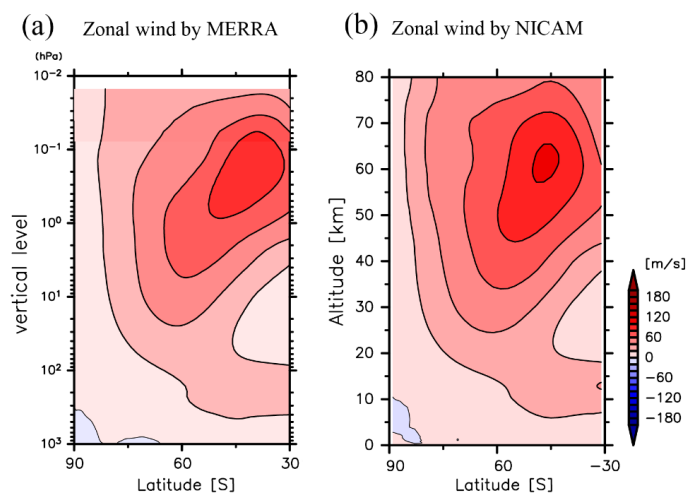
Figure 6: Latitude-altitude cross sections of the zonal mean zonal winds (a) from MERRA and (b) from NICAM simulations in May 2016. The contour intervals are 20 m s⁻¹.

1

2
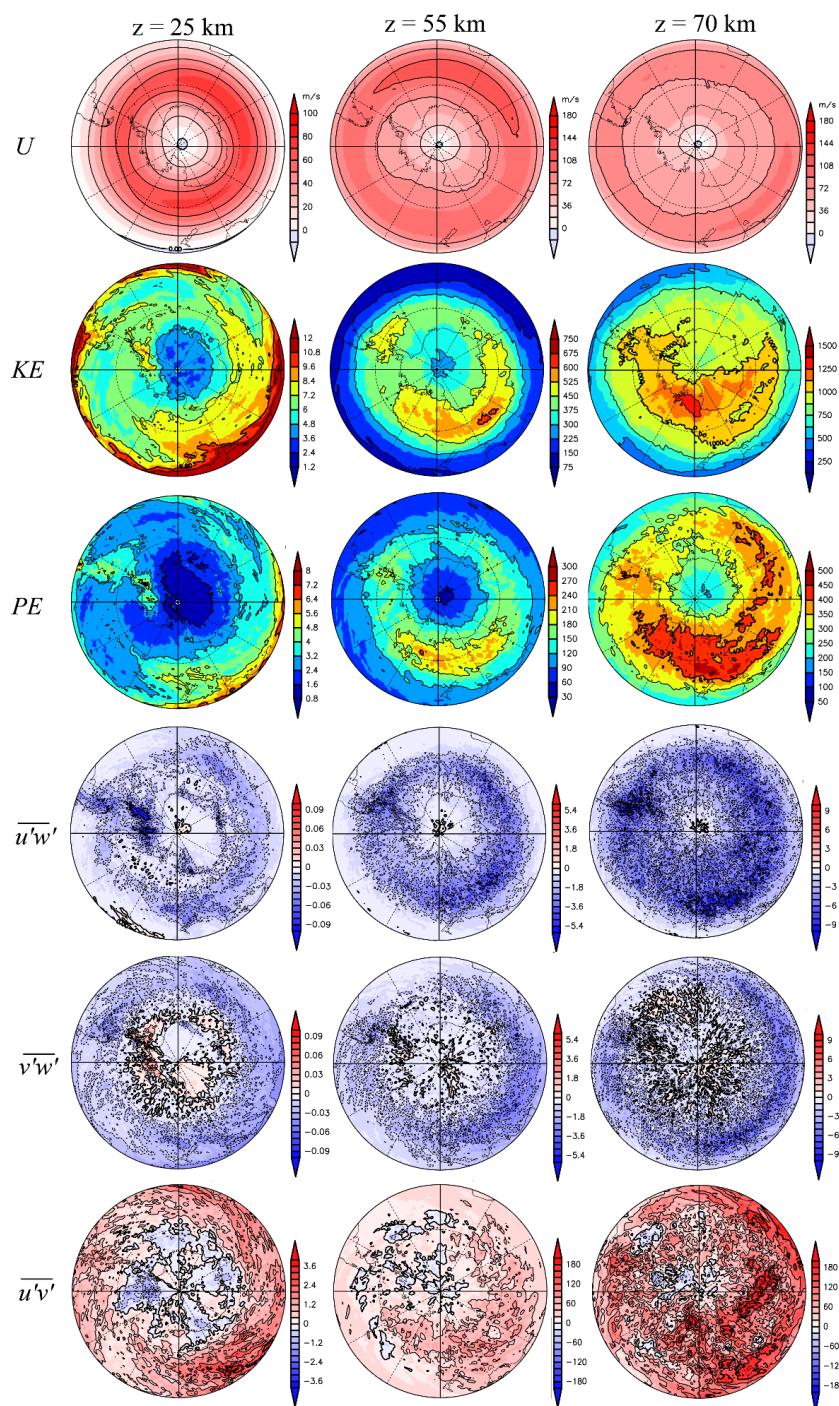
Figure 7: horizontal maps of U, $\overline{KE}$, $\overline{PE}$, $\overline{u'w'}, \overline{v'w'}$ and $\overline{u'v'}$ at heights of 25 km, 55 km and 70 km averaged in JJA. The unit of U, $\overline{KE}$ and $\overline{PE}$, and $\overline{u'w'}, \overline{v'w'}$ and $\overline{u'v'}$ is m s^{-1}, J/kg and m^{2}s^{-2}, respectively.
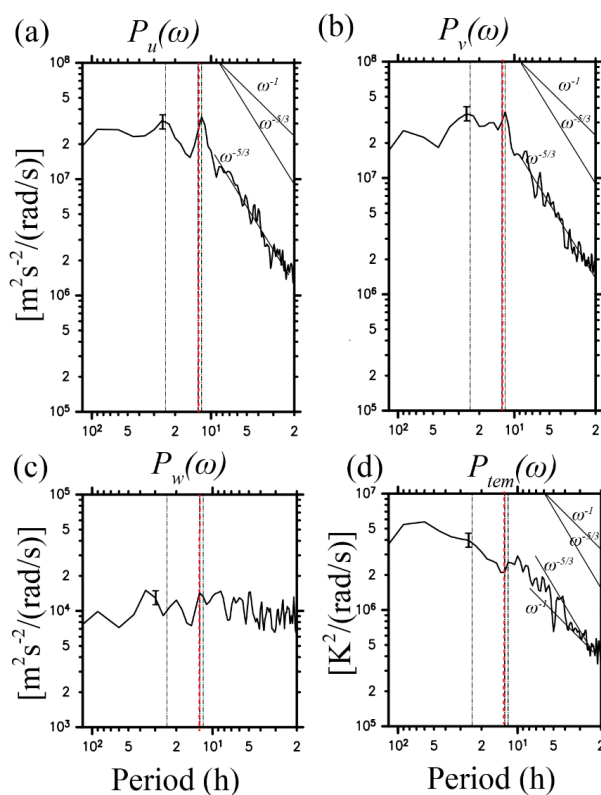
Figure 8: Frequency power spectra of (a) zonal, (b) meridional and (c) vertical wind, and (d) temperature fluctuations averaged for the height region of 70–75 km for JJA in NICAM at a grid point near Syowa Station. Vertical black dotted line indicates frequencies corresponding to the one day and half day. Red dotted line indicates the inertia-frequency at Syowa Station ($\sim 2\pi/12.7$ h at 69ºS). Error bars show intervals of the 90% statistical significance.

1

Atmospheric
Chemistry
and Physics
Discussions

1
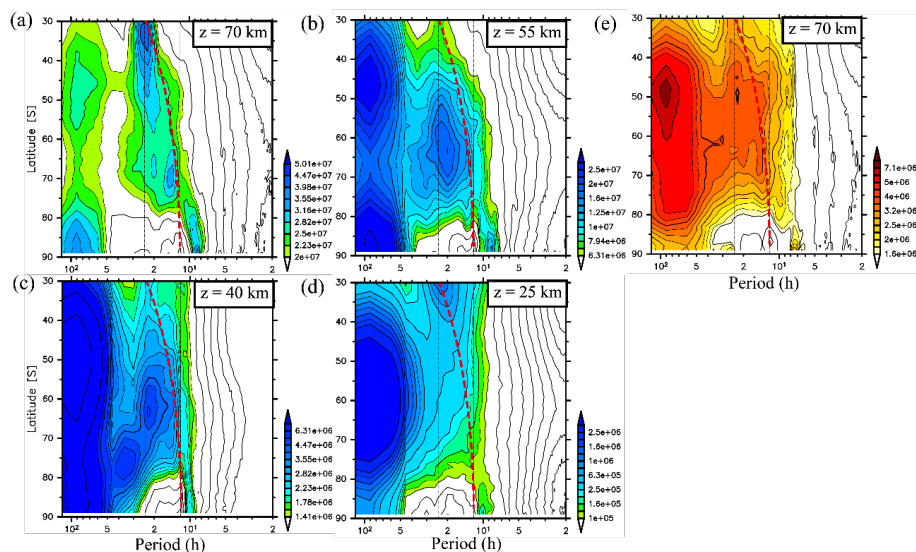
Figure 9: Zonal mean frequency power spectra of meridional wind fluctuations without diurnal and semi-diurnal migrating tides and semi-diurnal non-migrating tides with $s = 1$ $(\widetilde{P}_v(\omega))$ averaged in JJA as a function of latitude at heights of (a) 25 km, (b) 40 km, and (c) 55 km and (d) 70 km. (e) Frequency spectra of temperature fluctuations averaged in June and July with horizontal wavelengths longer than 1000 km without the migrating tides at 70 km. Vertical black dotted lines indicate frequencies corresponding to the one day period and half day. A red thick dashed curve indicates the inertial frequencies at each latitude.

2

3

1

(a) $\widetilde{P}_v(\omega)$ (70 km, 2π/30 h ~ 2π/12 h)　　(b) $\widetilde{P}_v(\omega)$ (70km, 2π/12 h ~ 2π/6 h)
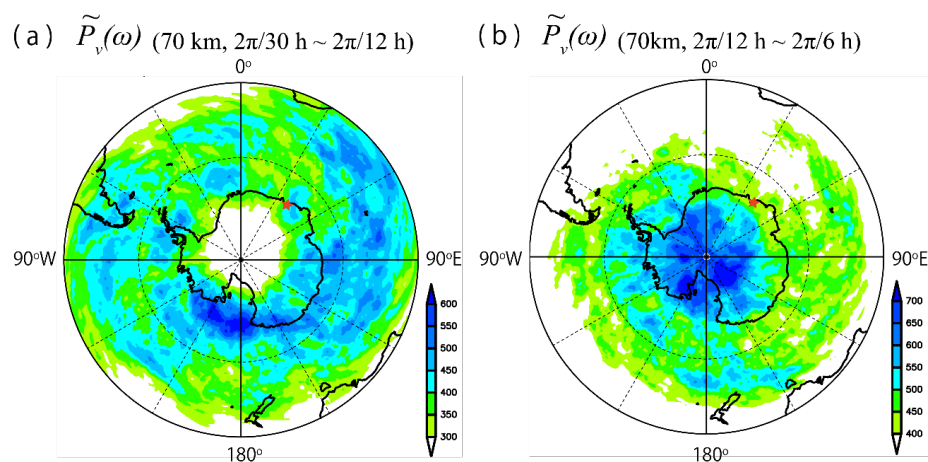
Figure 10: The horizontal map of $\widetilde{P}_v(\omega)$ contributed by disturbances (a) at the frequencies from (2π/30 h) to (2π/12 h) and (b) at the frequencies from (2π/12 h) to (2π/6 h) at a height of 70 km. A red star mark denotes a location of Syowa Station.
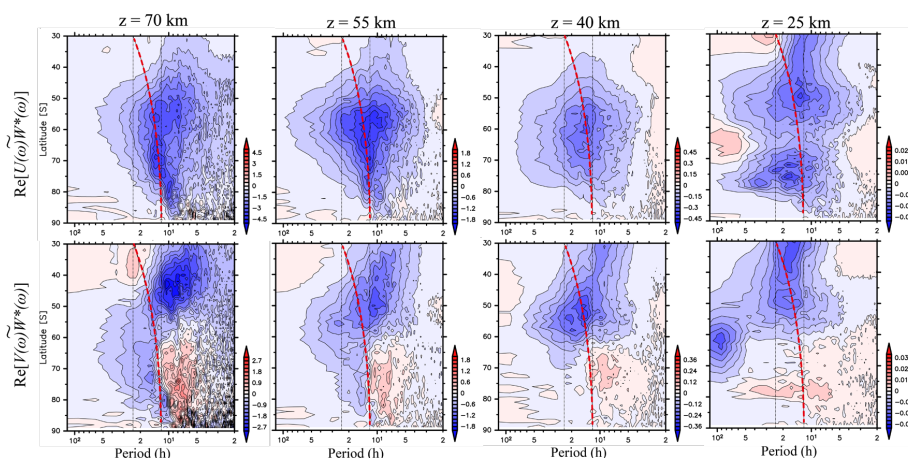
2

3

4

5

6

Atmospheric
Chemistry
and Physics
Discussions

Figure 11: Zonal mean frequency power spectra of vertical fluxes of zonal and meridional momentum

(Re[$U(\omega)W^*(\omega)$], Re[$V(\omega)W^*(\omega)$]) without diurnal and semi-diurnal migrating tides and semi-diurnal non-migrating tides with $s = 1$ averaged in JJA as a function of latitude at heights of 25 km, 40 km, 55 km and 70 km. Vertical black dotted lines indicate frequencies corresponding to the one day period and half day. A red thick dashed curve indicates the inertial frequencies at each latitude.
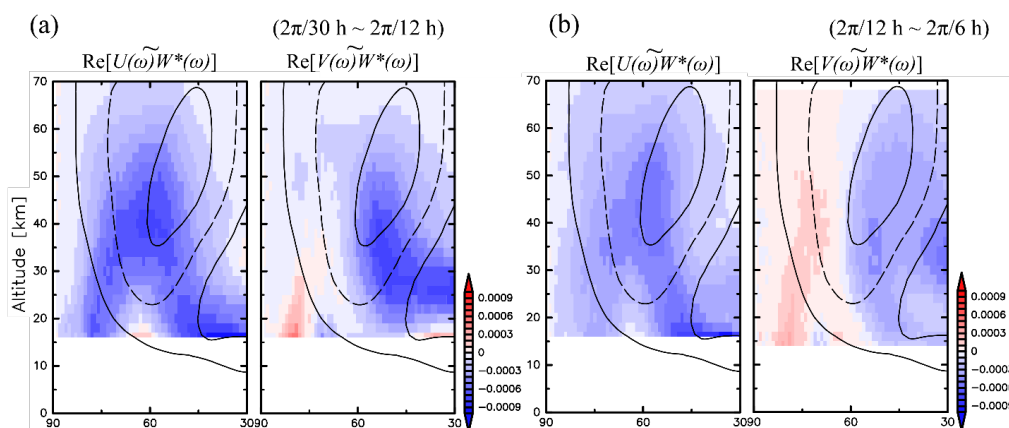
1

2

Figure 12: Latitudinal structures of an integration of $\text{Re}\left[\rho_0 U(\omega)\widetilde{W^*}(\omega)\right]$ and $\text{Re}\left[\rho_0 V(\omega)\widetilde{W^*}(\omega)\right]$ contributed by wave disturbances (a) for the frequencies from $(2\pi/30\ \text{h})$ to $(2\pi/12\ \text{h})$ and (b) for the frequencies from $(2\pi/12\ \text{h})$ to $(2\pi/6\ \text{h})$ averaged in JJA. The contour values indicate zonal mean zonal wind with a contour interval of 30 m s^{-1}.

1

2

(a) $\mathrm{Re}[U(\omega)\widetilde{W}^*(\omega)]$ (2π/30 h ~ 2π/12 h) (b) $\mathrm{Re}[U(\omega)\widetilde{W}^*(\omega)]$ (2π/12 h ~ 2π/6 h)
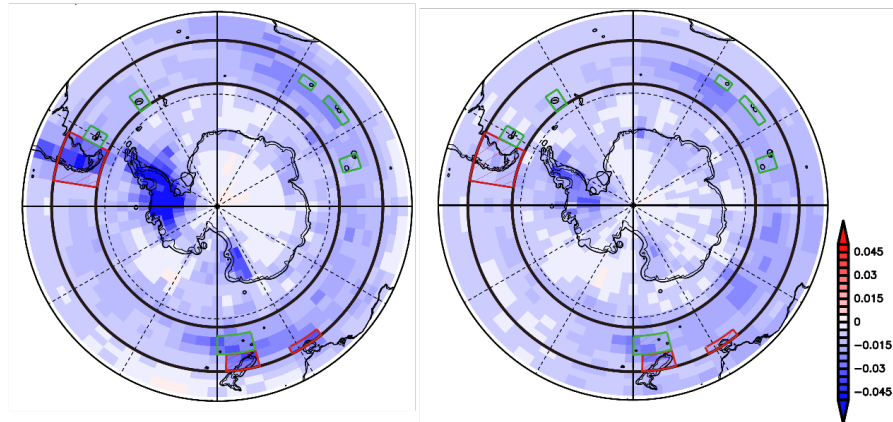

Figure 13: The horizontal map of $\mathrm{Re}\left[\rho_0 U(\omega)\widetilde{W}^*(\omega)\right]$ contributed by disturbances (a) at the frequencies from (2π/30 h) to (2π/12 h) and (b) at the frequencies from (2π/12 h) to (2π/6 h). Regions surrounded by red rectangles and green rectangles denote the domain dominated by the topography and the island, respectively.

1

2

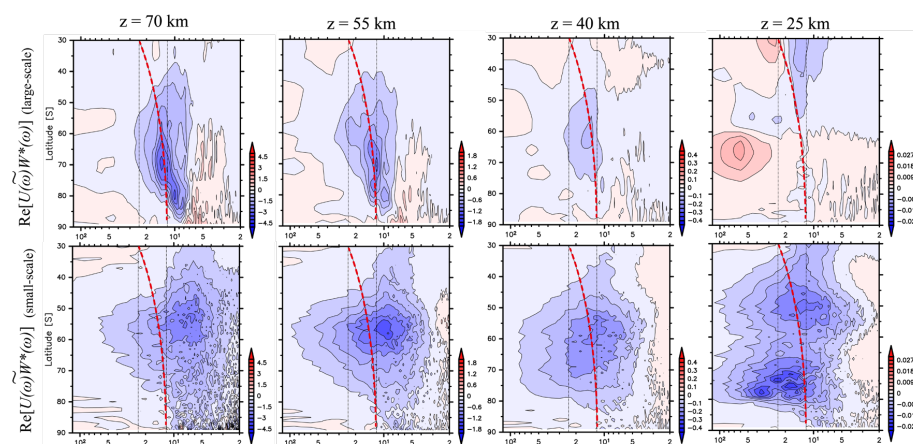Atmospheric
Chemistry
and Physics
Discussions

Figure 14: Zonal mean frequency power spectra of vertical fluxes of zonal momentum ($\mathrm{Re}[U(\omega)W^*(\omega)]$) without diurnal and semi-diurnal migrating tides and semi-diurnal non-migrating tides with $s = 1$ averaged in JJA as a function of latitude at heights of 25 km, 40 km, 55 km and 70 km. The upper (lower) line shows $\mathrm{Re}[U(\omega)W^*(\omega)]$ contributed by disturbances with horizontal scales larger (smaller) than 1000 km. A red thick dashed curve indicates the inertial frequencies at each latitude.

1

2

3